

## Behavior and punching capacity of flat slabs with the rational use of UHPFRC: NLFEA and analytical predictions

Sousa, Alex M.D. de; Lantsoght, Eva O.L.; Genikomsou, Aikaterini S.; Krah, Pablo A.; Debs, Mounir K. El

**DOI**

[10.1016/j.engstruct.2021.112774](https://doi.org/10.1016/j.engstruct.2021.112774)

**Publication date**

2021

**Document Version**

Accepted author manuscript

**Published in**

Engineering Structures

**Citation (APA)**

Sousa, A. M. D. D., Lantsoght, E. O. L., Genikomsou, A. S., Krah, P. A., & Debs, M. K. E. (2021). Behavior and punching capacity of flat slabs with the rational use of UHPFRC: NLFEA and analytical predictions. *Engineering Structures*, 244, Article 112774. <https://doi.org/10.1016/j.engstruct.2021.112774>

**Important note**

To cite this publication, please use the final published version (if applicable).  
Please check the document version above.

**Copyright**

Other than for strictly personal use, it is not permitted to download, forward or distribute the text or part of it, without the consent of the author(s) and/or copyright holder(s), unless the work is under an open content license such as Creative Commons.

**Takedown policy**

Please contact us and provide details if you believe this document breaches copyrights.  
We will remove access to the work immediately and investigate your claim.

# Behavior and punching capacity of flat slabs with the rational use of UHPFRC: NLFEA and analytical predictions

Alex D. de Sousa<sup>1,\*</sup>, Eva O.L. Lantsoght<sup>2,3</sup>, Aikaterini S. Genikomsou<sup>4</sup>, Pablo A. Krah<sup>5</sup>, Mounir El Debs<sup>6</sup>

1. Ph.D. student, University of São Paulo, São Carlos School of Engineering, São Carlos, Brazil

2. Full Professor, Politécnico, Universidad San Francisco de Quito, Quito, Ecuador

3. Assistant Professor, Delft University of Technology, Delft, the Netherlands

4. Assistant Professor, Queen's University, Ontario, Canada

5. Postdoctoral Researcher, University of Campinas, Campinas, Brazil

6. Emeritus Professor, University of São Paulo, São Carlos School of Engineering, São Carlos, Brazil

\*Corresponding author email: alex\_dantas@usp.br

## ABSTRACT

The outstanding mechanical properties of ultra-high-performance fiber-reinforced concrete (UHPFRC) can be used to improve the punching behavior of new slab-column connections. This study investigates the punching capacity of flat slab-column connections built with a rational combination of normal strength concrete (NSC) and UHPFRC in critical shear regions through non-linear finite element analyses (NLFEA) and by a punching shear model based on the critical shear crack theory (CSCT). Ten control tests from the literature were used to validate the Finite Element Models (FEM) developed to capture the behavior of slab-column connections made entirely with NSC, UHPFRC, and a combination of both materials. Parametric analyses were performed to investigate the behavior of connections with the rational use of UHPFRC, varying the reinforcement ratio, area, and thickness of the UHPFRC layer. The results indicated that placing a UHPFRC layer near the column in the slab compression zone significantly increases the punching capacity and deformation capacity compared to placing UHPFRC on the tensile side. The punching capacity enhancements varied between 26% and 156%, according to the reinforcement ratios and configurations of the UHPFRC layer investigated. The mean ratio between predicted punching capacities by advanced NLFEA and the analytical method proposed was 1.09, with a coefficient of variation of 10.3%. Therefore, the results indicated that the design of flat slabs with UHPFRC at the

critical shear regions is a viable solution. Finally, the CSCT model can be used in design to predict the punching capacity of these connections.

**Keywords:** Critical shear crack theory (CSCT); non-linear finite element analyses (NLFEA); punching shear capacity; rational use of the UHPFRC; slab-column connections.

## 1 INTRODUCTION

Ultra-high performance fiber-reinforced concrete (UHPFRC) is a cementitious material produced with Portland cement, pozzolans, small size aggregates, inert fillers, superplasticizer, and surface-treated steel fibers [1,2]. The outstanding properties of (i) high compressive strength [3–5], (ii) low permeability of the hardened composite, and (iii) high residual tensile strength compared to normal strength concrete (NSC) and steel fiber-reinforced concrete (SFRC) [6] make this material a promising solution to improve the punching capacity, durability, and deformation capacity of reinforced concrete (RC) flat slabs, and in particular slab-column connections [7–15]. For instance, in the case of RC beams failing in shear, experimental studies already showed that a total replacement of NSC by UHPFRC allowed increasing the normalized shear capacity by more than 70% and improved the deformation capacity at failure [16].

Although UHPFRC is more costly than NSC, its improved structural properties usually decrease the material consumption, reinforcement ratios, maintenance costs and increase the service life [17,18], which balance the overall cost of using UHPFRC for structural applications [6]. Traditionally, the main hurdle for spreading the use of UHPFRC as a building material for structural elements has been the lack of structural design guidance for this class of material [6]. Since the number of tests on slab-column connections built with UHPFRC is limited [7,9,14,19], the use of non-linear finite element analyses (NLFEA) could be a valuable tool to extend the knowledge about the behavior of such connections.

Several studies investigated numerical modeling approaches to predict the punching shear behavior of slab-column connections made entirely with NSC (NSC flat slabs) with and without shear

reinforcement [20–28]. In these, the NLFEA aided understanding and evaluating the effect of parameters such as openings close to the column on the structural response of flat slabs [22,29] and the compressive membrane action effect [24]. On the other hand, only a few studies described modeling approaches for using UHPFRC in slab-column connections [30,31]. In these studies [30,31], the UHPFRC was used only as an extra layer at the slab tensile side (strengthening material). The main acting forces were tangential stresses at the interface between the NSC and the UHPFRC and tensile forces induced by flexure at the UHPFRC layer. Therefore, these applications do not take advantage of the higher compressive strength of the UHPFRC compared to NSC. Moreover, there is a low number of numerical studies on using UHPFRC as the main material in the shear-critical regions [32,33].

At the same time, a reasonable amount of experimental studies investigated the punching capacity of slab-column connections designed with the rational use of advanced composites on the slab-column connection, such as SFRC [34–37] and ultra-high-performance concrete (UHPC – without fibers) [38,39]. Although UHPFRC combines the higher compressive strength of the UHPC and the higher residual tensile strength compared to the SFRC, only a few studies investigated the performance of slab-column connections with the rational use of UHPFRC at the shear-critical regions [14,40].

Therefore, the present study examines the behavior of flat slabs designed with the rational use of UHPFRC in shear-critical regions (Figure 1) aided by three-dimensional NLFEA. Moreover, parametric analyses investigate the influence of the (i) reinforcement ratio and (ii) geometry of the UHPFRC layer on the punching capacity of NSC-UHPFRC flat slabs. Since analytical methods are preferable in daily engineering for preliminary designs, this paper also proposes an analytical approach based on the critical shear crack theory (CSCT) [41] to assess the punching capacity of flat slabs designed with the rational use of UHPFRC.

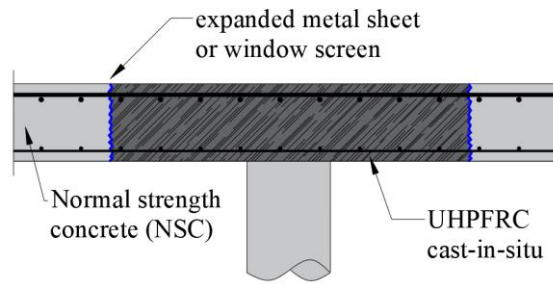


**Figure 1 – Detail of the slab-column connection with the rational use of UHPFRC (adapted from Moreillon [7]).**

Firstly, control slabs were used to validate the non-linear finite element models (FEM) developed. After that, a parametric study was conducted to investigate the influence of (i) the reinforcement ratio and (ii) different configurations of the UHPFRC layer on the punching capacity of NSC-UHPFRC flat slabs. In the end, the experimental control results, as well as the numerical results from the parametric analyses, were evaluated by the proposed analytical approach.

## **2 CONTROL SPECIMENS FROM LITERATURE**

### **2.1 Choice of control specimens**

All ten slab-column connections used in this study as control experiments were tested by Zohrevand et al. [14]. These specimens were chosen because they include three groups of specimens: (i) NSC flat slabs, (ii) UHPFRC flat slabs and (iii) flat slabs combining NSC and UHPFRC, with the last rationally used at the slab-column connection (NSC-UHPFRC flat slabs). Therefore, these tests allow validating separately the material models used to simulate the NSC and the UHPFRC. Moreover, the experimental program from Zohrevand et al. [14] also stood out by including specimens with high and lower reinforcement ratios (1.8% and 0.6%, respectively). Since flat slabs under punching loads may show different failure modes according to the reinforcement ratio, such as brittle punching failure or flexure-induced punching with reinforcement yielding [42], the selected control specimens allowed to validate the NLFEA under different failure mechanisms.

### **2.2 Geometry of control experiments**

Figure 2 shows the geometry of the control experiments tested by Zohrevand et al. [14]. The experimental program considered three groups of slabs: (i) fully made with NSC (C1.8 and C0.6,

where 1.8 and 0.6 refer to the reinforcement ratio of the slab); (ii) fully made with UHPFRC (U1.8 and U0.6) and (iii) hybrid slabs with the rational use of UHPFRC, which means that UHPFRC was used only on the slab-column connection area, while NSC was used for the remaining slab (Figure 2). Table 1 describes the geometry of the strengthened area with UHPFRC and the reinforcement ratio for the ten tests investigated in this study. Note that the specimens CU-A-F and CU-C-F used the UHPFRC layer over the entire thickness, while the specimens CU-B-H used UHPFRC only for half of the thickness.

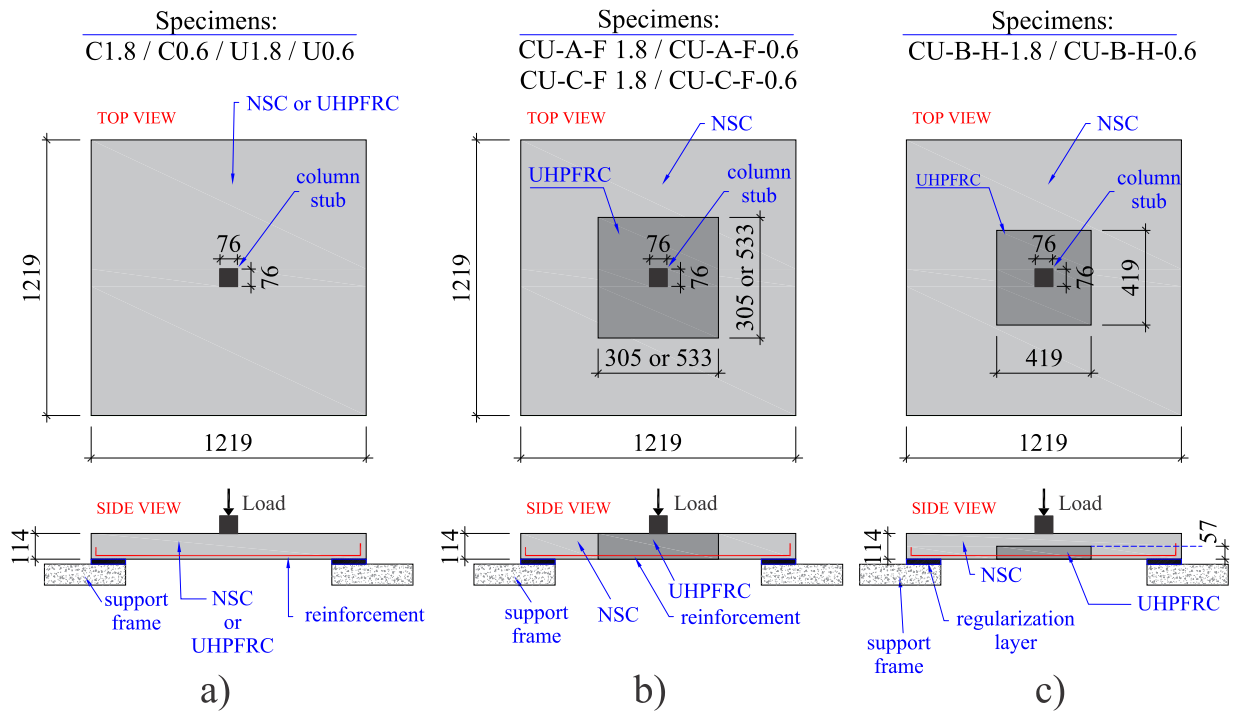


**Figure 2 – a) Geometry of the slabs tested by Zohrevand et al. [14]: a) specimens fully made of NSC or UHPFRC; b) specimens with the rational use of UHPFRC over the full depth of the slabs and c) specimens with UHPFRC limited to only half of the slab thickness. (All dimensions are in mm).**

All slabs were square with 1219 mm × 1219 mm in plan and with 114 mm of thickness. These slabs were loaded at the center on an area of 76 mm × 76 mm. Each specimen was supported on rigid frames over a length of 152.5 mm on all four sides free to lift. At the interface between the slabs and the rigid frame, the authors [14] described using a gypsum cement layer to level the slabs over the support. Moreover, some figures also indicated the use of a thin, flexible plastic sheet between the

slabs and the supports. No information was reported about the stiffness and thickness of these materials and where they were applied, which required additional attention in this numerical study.

**Table 1 - Geometry of the control slabs**

Model Identification	Geometry of the UHPFRC layer (mm)	$\rho_l$ (%)	$\rho_t$ (%)	$\rho$ (%)
C1.8	-	1.70	1.97	1.8
C0.6	-	0.56	0.65	0.6
U1.8	-	1.70	1.97	1.8
U0.6	-	0.56	0.65	0.6
CU-A-F-1.8	$533 \times 533 \times 114$	1.70	1.97	1.8
CU-A-F-0.6	$533 \times 533 \times 114$	0.56	0.65	0.6
CU-C-F-1.8	$305 \times 305 \times 114$	1.70	1.97	1.8
CU-C-F-0.6	$305 \times 305 \times 114$	0.56	0.65	0.6
CU-B-H-1.8	$419 \times 419 \times 57$	1.70	1.97	1.8
CU-B-H-0.6	$419 \times 419 \times 57$	0.56	0.65	0.6

**Note:**  $\rho_l$  and  $\rho_t$  denote the reinforcement ratios of the slabs in the longitudinal and transversal directions. The longitudinal reinforcement is associated with the higher effective depth.  $\rho$  is the mean reinforcement ratio calculated as  $\rho = (\rho_l \cdot \rho_t)^{1/2}$ .

### 2.3 Material properties of control slabs

Table 2 describes the material properties of the concretes used in the tests. The main properties of the UHPFRC reported are the measured tensile and compressive strengths on cylindrical specimens ( $102 \text{ mm} \times 203 \text{ mm}$ ) with traditional compressive and splitting tensile tests, respectively. Therefore, no information is available about the hardening and softening behavior of UHPFRC under tension and compression. Several batches were used to cast the UHPFRC-slabs and hybrid slabs, with their 28-day compressive strength ranging from 129 MPa to 151 MPa. The tensile strength of the UHPFRC varied between 6 MPa and 10 MPa for the different batches, with an average value of 8 MPa [14]. A single batch of NSC was used for the control slabs, with an average compressive strength of 45 MPa and coarse aggregate with a maximum size of 9.5 mm. The tensile strength of the NSC-batch was not reported.

Straight steel fibers were used in the UHPFRC mix. These copper-coated micro steel fibers were 13-mm long with a diameter of 0.2 mm and tensile strength of 2800 MPa. The reinforcement of the slabs consisted of N° 13M steel bars spaced at 76 mm ( $\rho = 1.8\%$ ) and 229 mm ( $\rho = 0.6\%$ ) on

center. The reinforcement was placed in two orthogonal directions on the tension side of the slab, with a clear cover of 13 mm. The yield strength of the reinforcement was 414 MPa [14].

**Table 2 – Material properties described in reference [14].**

Concrete	NSC		UHPFRC					
Model Identification	$f_{cm}$ (MPa)	$d_{ag}$ (mm)	$f_{cm}$ (MPa)	$f_{ct}$ (MPa)	$V_f$ (%)	$l_f$	$f_{y,fiber}$ (MPa)	$d_f$ (mm)
C1.8	45	9.5	-	-	-	-	-	-
C0.6			-	-	-	-	-	-
U1.8	45	9.5	128.6	AVG = 8 MAX = 10 MIN = 6	2	13	2800	0.2
U0.6			136.8					
CU-A-F-1.8			150.3					
CU-A-F-0.6			151.4					
CU-C-F-1.8			147.4					
CU-C-F-0.6			139.7					
CU-B-H-1.8			139.7					
CU-B-H-0.6			139.7					

### 3 FINITE ELEMENT SIMULATIONS

#### 3.1 Overview

The finite element software ABAQUS/CAE [43] was used to model the control slabs. By considering specimens' symmetry, a quarter of the slabs was modeled to reduce the computational effort (Figure 3a).

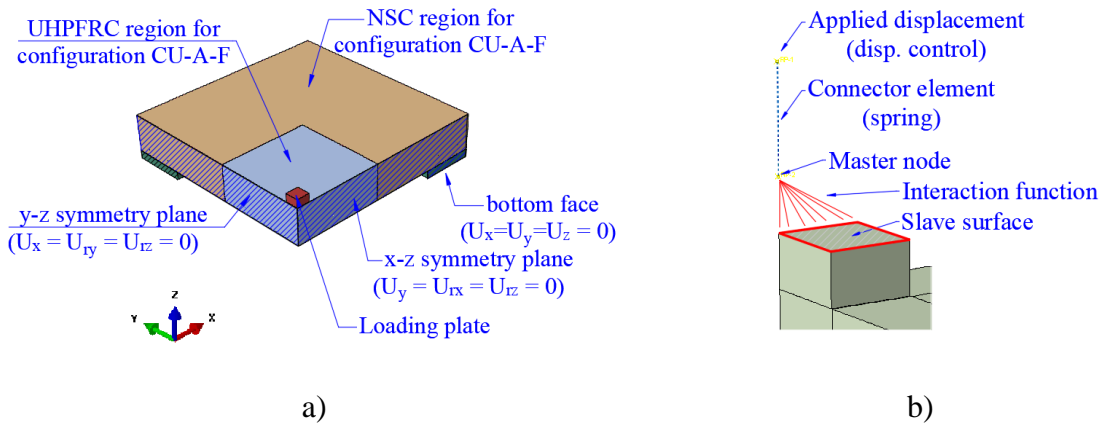


**Figure 3 – Details of the boundary conditions used: a) overview of the model and b) detail of the displacement-controlled loading.**

In all analyses, the load was applied in displacement-controlled conditions in order to evaluate the governing punching failure mode. To make a fair comparison between experimental and numerical results in terms of force-displacement graphs, due to the uncertainties in slab-support

interactions and loading protocol, a spring was coupled to the loading plate of the numerical models (Figure 3b) and its stiffness was calibrated to reproduce the initial stiffness of the experimental results. In this study, it is assumed that the graphs reported in reference [14] were influenced by the calibration of the actuator and by soft materials between the frame support and the slab surface based on the test pictures [14].

### **3.2 Boundary Conditions**

Zohrevand et al. [14] described that the specimens were leveled between the bottom slab surface and the rigid support frame using gypsum cement layers. The same material was also used between the loading plate and the slab surface to ensure a vertical concentric load. However, pictures of the specimens also show a thin, flexible plastic sheet between the slab and the rigid support frame. Based on this information, a soft material layer between the slabs and the rigid frame was assumed. In this study, instead of modeling the full support frame, only a support layer of 25 mm in thickness was modeled, and a small value of Young's modulus (4 MPa) was assigned to this material to simulate the soft material between the slab and the support in the tests.

### **3.3 Interfaces**

Since the NSC and UHPFRC interface did not show any signal of damage or crack opening in the tests, a rigid interaction (perfect bond) between NSC and UHPFRC (no sliding) was assumed. Other experimental studies also support the outstanding bonding properties between UHPFRC and NSC [44–47]. The interface between the support frame and loading block surface with the slab was modeled assuming (i) hard contact (allowing separation of the surfaces) and (ii) frictionless. As no anchorage failure was reported in the experiments and the main aim of the numerical model was to predict the punching capacity, bond-slip was not considered in the simulations and a perfect bond between reinforcement and concrete was assumed.

### **3.4 Mesh and Procedure of solution**

Concrete, supporting pad and loading plates were simulated with 8-node hexahedral solid elements with reduced integration (C3D8R). Reduced integration was used to avoid the shear locking

of the brick elements based on the Reissner-Mindlin theory [43,48]. For solid elements, hourglass control has also been activated to avoid distortion associated with mesh discretization and linear approximation for the element displacement field. The reinforcement was modeled with 2-node truss elements (T3D2).

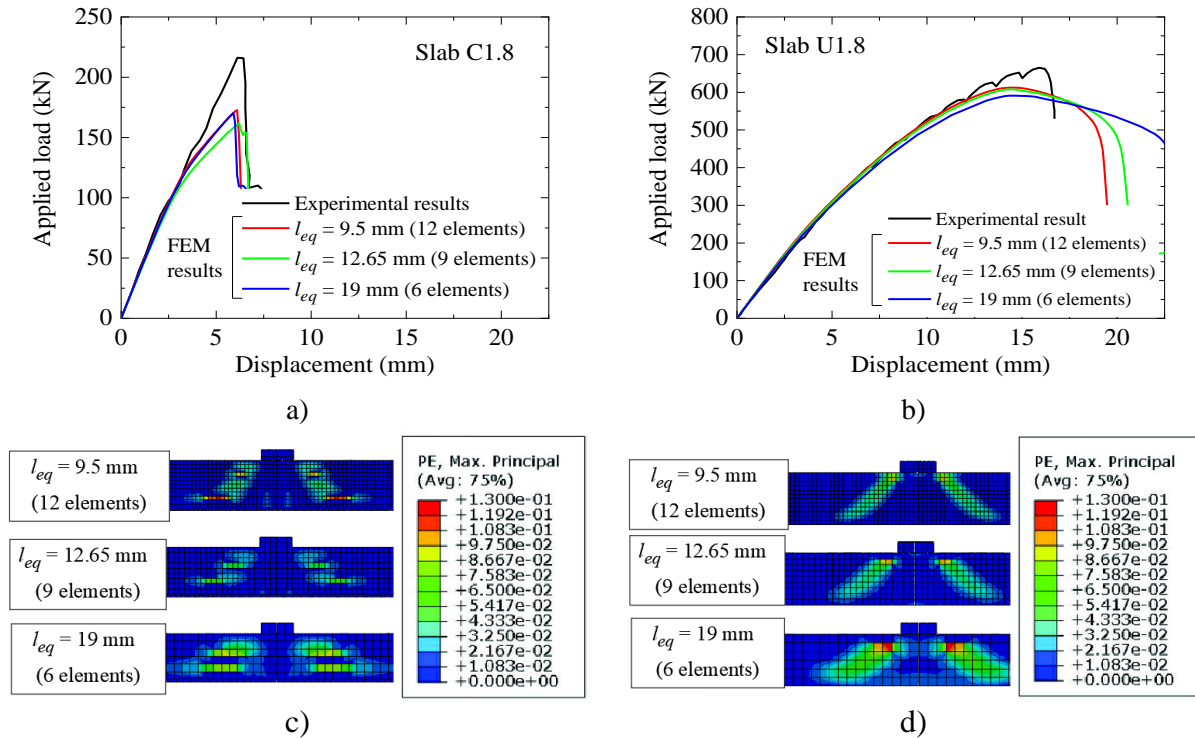


**Figure 4 – Behavior in term of the applied load versus mid-span displacement according to the finite element size for: (a) slab C1.8, and (b) slab U1.8; comparison of the cracking patterns predicted by the FEM (herein evaluated through the qualitative distribution of the maximum principal plastic strains) according to the finite element size: c) slab C1.8 and d) slab U1.8.**

Figure 4 shows the summary of the mesh sensibility study performed, which comprehended the slabs C1.8, C0.6, U1.8 and U0.6. Here, only the results from the slabs C1.8 and U1.8 are described as the findings from C0.6 and U0.6 are similar. Figure 4 shows that the governing failure mode and global response of the FEM did not change significantly with the mesh discretization due to the consistency of the material models adopted (Section 3.5). The finite element size was chosen as 9.5 mm, which allows having 12 elements over the thickness of the slab model. Despite requiring a higher time to perform the numerical analyses, the finer mesh discretization allowed tracking the cracking

pattern evolution from the FEM and better represented the post-peak behavior from the load versus mid-span displacement graphs (Figure 4b).

Figure 5a shows the mesh discretization of two models, highlighting the areas of UHPFRC and NSC in different colors. A more refined mesh discretization was required to allow varying the thickness of the UHPFRC layer in the parametric study (Section 7), assuring at least three elements over the UHPFRC layer thickness (Figure 5b).

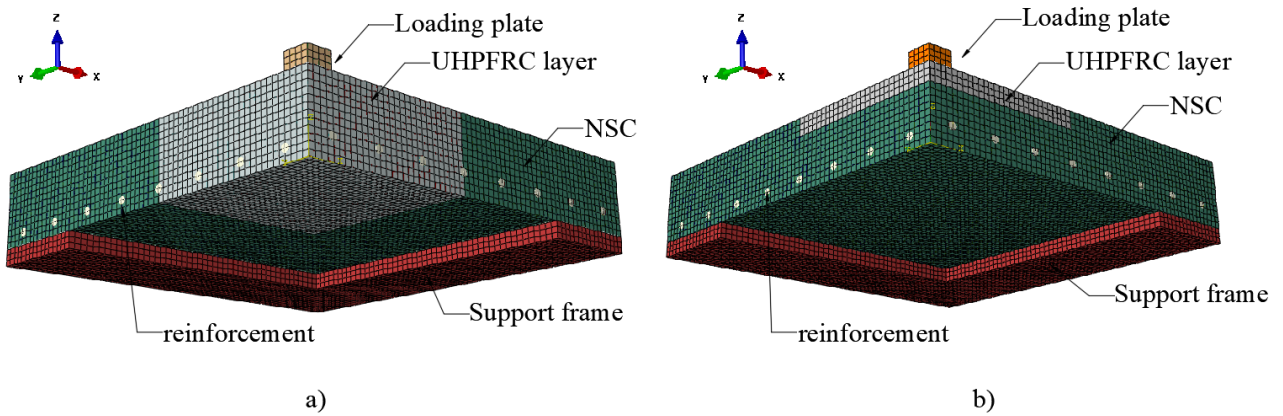


**Figure 5 – Mesh discretization of a) slab CU-A-F-18 and b) example of a slab with a small thickness of the UHPFRC layer on the compression side used in the parametric study (Section 7). Note: Only a quarter was modeled.**

### 3.5 Material modeling

Table 3 shows the material models used for describing the stress-strain behavior of NSC under compression [49] and tension [50]. The model of Hordijk [50] considers the crack bandwidth length  $l_{eq}$  to reduce the mesh sensitivity through the same approach described by Genikomsou and Polak [20].

Table 4 shows the damage evolution models used for the NSC. The model of Alfarah et al. [51] was chosen since it accounts for the bandwidth length  $l_{eq}$  in tension. Therefore, this model can reduce mesh sensitivities due to tension cracking.

**Table 3 – Stress-strain behavior models for NSC.**

Tension behavior – Hordijk [50]	$\frac{\sigma_t(w)}{f_{ct}} = \left[ 1 + \left( c_1 \cdot \frac{w}{w_c} \right)^3 \right] \cdot e^{-c_2 \cdot \frac{w}{w_c}} - \frac{w}{w_c} \cdot (1 + c^3) \cdot e^{-c_2} \quad (1)$ <p>With: <math>c_1 = 3</math>; <math>c_2 = 6.93</math>; <math>w_c</math> is the critical crack opening or fracture crack opening:</p> $w_c = 5.14 \cdot \frac{G_f}{f_{ct}} \quad (2)$ <p>The tensile strain after cracking can be described in terms of the crack opening from the following kinematic relation:</p> $\varepsilon_t = \frac{f_{ct}}{E_c} + \frac{w}{l_{eq}} = \varepsilon_{t,cr} + \frac{w}{l_{eq}} \quad (3)$
Compression behavior – Carreira and Chu [49]	$\frac{\sigma_c(\varepsilon)}{f_{cm}} = \frac{\beta_{cc} \cdot (\varepsilon / \varepsilon_{c1})}{\beta_{cc} - 1 + (\varepsilon / \varepsilon_{c1})^\beta} \quad (4)$ $\beta_{cc} = \frac{1}{1 - \frac{f_{cm}}{\varepsilon_{c1} \cdot E_c}} \quad (5)$

**Table 4 – Damage evolution laws used for NSC.**

Reference	Tension damage
Alfarah et al. [51]	$d_t = 1 - \frac{1}{2 + a_t} \left[ 2(1 + a_t) \exp(-b_t \varepsilon_t^{pl}) - a_t \exp(-2b_t \varepsilon_t^{pl}) \right] \quad (6)$
	Compression damage
Birtel and Mark [52]	$d_c = 1 - \frac{\sigma_c \cdot E_c^{-1}}{\varepsilon_c^{pl} \cdot (1/b_c - 1) + \sigma_c \cdot E_c^{-1}} \quad (7)$

Table 5 shows the proposed stress-strain models used to describe the behavior of UHPFRC under tension and compression. The only available information about the UHPFRC, despite the volume fraction and material properties of the fibers, are the average tensile strength and the compressive strength for each batch. In the absence of detailed information about the strain-hardening behavior, UHPFRC was assumed as a strain-softening material in tension using the stress-crack opening relationship described by Fehling et al. [1]. The parameter  $\sigma_{cft0}$  was assumed equal the peak

tensile strength of the UHPFRC. In compression, the model of Carreira and Chu [49] modified by Mansur et al. [53] was considered, as used in Krahel et al. [2].

**Table 5 - Stress-strain behavior models used for UHPFRC.**

Reference	Tension behavior
Fehling et al. [1].	$\sigma_t(w) = \sigma_{cf0} \cdot \left(1 - 2 \cdot \frac{w}{l_f}\right)^2 \quad (8)$
	Compression behavior
Carreira and Chu [49] modified by Mansur et al. [53]	$\frac{\sigma_c(\varepsilon)}{f_{cm}} = \frac{k_1 \cdot \beta_{cc} \cdot (\varepsilon_c / \varepsilon_{c1})}{k_1 \cdot \beta_{cc} - 1 + (\varepsilon_c / \varepsilon_{c1})^{k_2 \cdot \beta_{cc}}} \quad (9)$
	$\beta_{cc} = \frac{1}{1 - \frac{f_{cm}}{\varepsilon_{c1} \cdot E_c}} \quad (10)$
	$k_1 = \left(\frac{50}{f_{cm}}\right)^3 \cdot \left[1 + 2.5 \cdot \left(\frac{\rho_f \cdot l_f}{d_f}\right)^{2.5}\right] \quad (11)$
	$k_2 = \left(\frac{50}{f_{cm}}\right)^{1.3} \cdot \left[1 - 0.11 \cdot \left(\frac{\rho_f \cdot l_f}{d_f}\right)^{-1.1}\right] \quad (12)$

The models from Krahel et al. [4] and Alfarah et al. [51] were used to describe the damage evolution laws under compression and tension for the UHPFRC, respectively (Table 6).

**Table 6 – Damage evolution laws used for UHPFRC.**

Reference	Tension damage
Alfarah et al. [51]	$d_t = 1 - \frac{1}{2 + a_t} \left[ \frac{2(1 + a_t) \exp(-b_t \varepsilon_t^{ck})}{-a_t \exp(-2b_t \varepsilon_t^{ck})} \right] \quad (13)$
	Compression damage
Krahel et al. [4]	$d_c = (\tanh(m \cdot \varepsilon_c)) \cdot (r \cdot \exp(-n \cdot \varepsilon_c)^k) \quad (14)$ For $\rho_f = 2\%$ : $m = 106.2$ ; $n = 188.5$ ; $k = 3.05$ ; $r = 0.93$

### 3.6 Plasticity parameters

The parameters used for NSC were chosen based on the literature review [20,21,24,25,28,48]. The dilation angle adopted for NSC was 30°. Notably, this value is close to that expected by Poliotti and Bairan [54] for the maximum dilation angle of NSC ( $\Psi = 32^\circ$ ) based on inverse analyses of

experimental investigations. The fracture energy adopted for NSC was calculated according to the *fib* Model Code 2010 [55] since the values with the Model Code 1990 [56] underestimated the punching capacity of the numerical models. The default value of the ratio  $\sigma_{b0}/\sigma_{c0}$  in ABAQUS is 1.16 for NSC. This value is based on the experimental tests of Kupfer et al. [57,58]. However, it should be highlighted that this value was found for NSC with a concrete compressive strength lower than 60 MPa.

The parameters used for the UHPFRC were mainly based on inverse analyses of experimental results proposed by Krahel et al. [2]. The higher dilation angle used for UHPFRC was based on reverse analysis of triaxial tests [59,60]. However, other experimental investigations with triaxial tests also support that higher dilation angles for UHPFRC than for NSC are suitable since the addition of fibers and the better matrix packing allows increasing the toughness of the concrete [61,62]. For UHPFRC specimens, where the fibers induce more toughness in compression, Krahel et al. [2] found a value of  $\sigma_{b0}/\sigma_{c0} = 1.07$  based on the tests of Speck [59] (compression-compression tests) and Lee et al. [63] (tension-compression tests).

### 3.7 Summary of the material parameters of the reference FEM

In order to ease the identification of the material parameters used in the reference finite element models, Table 7 summarized the main information of the materials models used for the stress-strain behavior and damage evolution of NSC and UHPFRC.

**Table 7 – Concrete damaged plasticity (CDP) model parameters used for the reference numerical analyses.**

Parameter	NSC	UHPFRC
<b>Yield criterion</b>		
Compressive behavior ( $\sigma_c \times \varepsilon_c$ )	Carreira and Chu [49]	Mansur et al. [53]
Tensile behavior ( $\sigma_t \times \varepsilon_t$ )	Hordijk [50]	Fehling et al. [1].
<b>Damage evolution</b>		
Compression damage ( $d_c \times \varepsilon_c^{in}$ )	Birtel and Mark [52]	Krahel et al. [4]
Tensile damage ( $d_t \times \varepsilon_t^{ck}$ )	Alfarah et al. [51]	Alfarah et al. [51]
<b>Plasticity parameters</b>		
Dilation angle, $\Psi$ ( $^\circ$ )	30	54 [2]
$\sigma_{b0}/\sigma_{c0}$	1.16 [57,58]	1.07 [2]
Parameter $K_c$	0.66 [43]	0.66 [2]

Eccentricity, $e$	0.1	0.1
Viscosity parameter, $\mu$	0.00001	0.00001
Fracture energy, $G_f$	Model Code 2010	-
$f_{ct}$	Model Code 2010	Hoang and Fehling [67]

The stress-inelastic strain values used for NSC (slab C1.8) and UHPFRC (slab U1.8) are listed in Table 8, as provided in other numerical studies [64,65]. In order to avoid numerical convergence problems, the maximum value for the damage parameters was assumed as 0.9, which is also consistent with experimental measurements from this variable for both materials [4,66].

**Table 8 - Parameters required to define the stress-strain behavior of NSC and UHPFRC under compression and tension in the CDP (values used for slabs C1.8 and U1.8).**

Compression behavior of NSC			Tension behavior of NSC		
Compressive stress (MPa)	Inelastic strain (-)	Damage parameter (-)	Tensile stress (MPa)	Inelastic strain (-)	Damage parameter (-)
18.00	0.00000	0.000	3.80	0.00000	0.0000
30.17	0.00009	0.029	2.69	0.00106	0.2545
38.99	0.00027	0.067	1.94	0.00212	0.4640
43.69	0.00057	0.120	1.27	0.00369	0.6846
45.00	0.00098	0.183	0.85	0.00576	0.8495
44.00	0.00146	0.256	0.65	0.00783	0.9000
35.82	0.00306	0.470	0.50	0.00990	0.9000
29.02	0.00440	0.611	0.37	0.01197	0.9000
18.41	0.00744	0.807	0.26	0.01404	0.9000
8.84	0.01410	0.900	0.16	0.01611	0.9000
2.70	0.03523	0.900	0.08	0.01817	0.9000
Compression behavior of UHPFRC			Tension behavior of UHPFRC		
Compressive stress (MPa)	Inelastic strain (-)	Damage parameter (-)	Tensile stress (MPa)	Inelastic strain (-)	Damage parameter (-)
99.43	0.000000	0.0000	7.64	0.00000	0.00000
112.73	0.000023	0.0000	7.04	0.02737	0.23729
123.69	0.000086	0.0056	6.47	0.05474	0.43850
128.60	0.000266	0.0154	5.92	0.08211	0.59539
107.13	0.002873	0.2312	4.89	0.13684	0.79736
57.96	0.007109	0.6373	3.53	0.21895	0.90000
34.21	0.010857	0.7805	2.40	0.30105	0.90000
22.45	0.014373	0.8523	1.48	0.38316	0.90000
14.36	0.018915	0.8985	0.60	0.49263	0.90000
10.90	0.022272	0.9000	0.20	0.57474	0.90000
8.58	0.025607	0.9000	0.01	0.65684	0.90000

## 4 ANALYTICAL PREDICTIONS WITH MECHANICAL-BASED MODELS

### 4.1 CSCT-based model for SFRC

The punching shear capacities of the control slabs [14], as well as those predicted by the FEM developed in the parametric study (Section 7), were compared to those provided by the CSCT developed by Muttoni [41] and modified by Maya et al. [68] to cover SFRC flat slabs. In this model, the punching capacity is calculated by:

$$P_{R,CSCT} = P_{R,c,CSCT} + P_{R,f,CSCT} \quad (15)$$

where,  $P_{R,c,CSCT}$  and  $P_{R,f,CSCT}$  are the contribution of the concrete and the fibers to the punching capacity, respectively [68]. The contribution of concrete, which represents the failure criterion of NSC flat slabs without transverse reinforcement, can be calculated as [68]:

$$P_{R,c,CSCT} = \frac{3/4 \cdot \sqrt{f_{cm}}}{1 + 15 \cdot \frac{\psi_{CSCT} \cdot d}{d_{g0} + d_{ag}}} \cdot (b_0 \cdot d) \quad (16)$$

where,  $\psi_{CSCT}$  is the slab rotation at failure;  $d$  is the effective depth of the slab;  $b_0$  is the control perimeter at a distance of  $d/2$  from the face of the column;  $f_{cm}$  is the average compressive strength of the concrete;  $d_{ag}$  is the maximum aggregate size of the concrete, and  $d_{g0}$  is a reference aggregate size set to 16 mm [68]. For symmetrical slab-column connections, the rotation  $\psi_{CSCT}$  at failure can be estimated according to the provisions of *fib* Model Code 2010 at the Level of Approximation III [55,69,70]:

$$\psi_{CSCT} = 1.2 \cdot \frac{r_s}{d} \cdot \frac{f_y}{E_s} \cdot \left( \frac{P}{P_{flex}} \right)^{3/2} \quad (17)$$

with  $r_s$  equal to the distance from the column axis to the line of contra-flexure of the bending moments,  $f_y$  the average yield strength of the flexural reinforcement, and  $E_s$  the modulus of elasticity of the longitudinal reinforcement [41]. The flexural capacity  $P_{flex}$  for the square slabs tested by Zohrevand, as well the slabs in the parametric analysis, was calculated as suggested by Zohrevand et al. [14]:

$$P_{flex} = 8 \cdot m_R \cdot \left( \frac{1}{1 - \frac{c_{load}}{B}} - 3 + 2\sqrt{2} \right) \quad (18)$$

where  $B$  and  $c_{load}$  are the dimensions of the slab and plate load, respectively (both in mm);  $m_R$  is the average flexural strength per unit width in the support strip. The yield flexural strength per unit width  $m_R$  for SFRC, which includes the contribution of the fibers, is calculated as [68,71]:

$$m_R = \rho \cdot d^2 \cdot f_y \cdot \left[ 1 - \frac{\beta_1 \cdot (\rho \cdot f_y + f_{ct2,f} \cdot h / d)}{2 \cdot (\alpha_{cc} \cdot f_{cm} + f_{ct2,f})} \right] + h^2 \cdot \frac{f_{ct2,f}}{2} \cdot \left[ 1 - \frac{\rho \cdot f_y \cdot d / h + f_{ct2,f}}{(\alpha_{cc} \cdot f_{cm} + f_{ct2,f})} \right] \cdot \left[ 1 + \frac{\rho \cdot f_y \cdot d / h + f_{ct2,f}}{\alpha_{cc} \cdot f_{cm} + f_{ct2,f}} \cdot (1 - \beta_1) \right] \quad (19)$$

In the simplified form [68], the contribution of the fibers  $P_{R,f,CSCT}$  to the punching capacity can be calculated as [68]:

$$P_{R,f,CSCT} = A_p \cdot \sigma_{tf} \quad (20)$$

In Eq. (20),  $A_p$  is the horizontally projected area of the punching failure surface and  $\sigma_{tf}$  is the fiber bridging stress, which can be calculated according to the Variable Engagement Model [72]:

$$\sigma_{tf} = K_f \cdot \alpha_f \cdot \rho_f \cdot \tau_b \quad (21)$$

where  $K_f$  is the global orientation factor;  $\rho_f$  is the fiber volume content;  $\tau_b$  is the bond stress between the fibers and the concrete matrix, and  $\alpha_f$  is the fiber slenderness, defined as the ratio between the length ( $l_f$ ) and diameter ( $d_f$ ) ( $\alpha_f = l_f / d_f$ ) [68]. According to Voo and Foster [72,73],  $K_f$  can be estimated by:

$$K_f = \frac{1}{\pi} \arctan \left( \alpha_e \cdot \frac{w}{d_f} \right) \cdot \left( 1 - \frac{2}{l_f} \right)^2 \quad (22)$$

where  $\alpha_e$  is defined as an engagement parameter that can be taken as  $\alpha_e = 3.5$ . According to Maya et al. [68], the interfacial bond strength between the matrix and the fiber  $\tau_b$  is given by:

$$\tau_b = k_b \cdot \sqrt{f_{cm}} \quad (23)$$

## 4.2 Proposed approaches for UHPFRC and NSC-UHPFRC flat slabs

The equations developed to calculate the unitary flexural capacity of SFRC flat slabs could underestimate the flexural capacity of UHPFRC slabs due to the lower residual tensile strength from the SFRC compared to the UHPFRC. In this way, a set of equations, based on the work from Fehling et al. [1], was devised for estimating the unitary moment capacity  $m_{R1}$  of slab cross-sections with UHPFRC distributed over (i) the full depth, (ii) at the tension side and (iii) at the compression side of the slabs (Table 9).

**Table 9 - Equations for estimating the compression zone depth ( $x$ ) and unitary moment capacity ( $m_{R1}$ ) for sections with different distributions of UHPFRC over the thickness.**

Full depth	
$x = A_s \cdot f_y + 0.81 \cdot h_{slab} \cdot b_w \cdot f_{Ftu} / (0.5 \cdot b_w \cdot f_{c,UHPFRC} + 0.81 \cdot b_w \cdot f_{Ftu})$ $m_{R1} = 0.5 \cdot x \cdot b_w \cdot f_{c,UHPFRC} \cdot \left(d - \frac{x}{3}\right) - 0.81 \cdot (h - x) \cdot b_w \cdot f_{Ftu} \cdot (d - 0.45 \cdot x - 0.55 \cdot h) \quad (24)$	
Tension side	
$x = A_s \cdot f_y + 0.81 \cdot h_{slab} \cdot b_w \cdot f_{Ftu} / (0.5 \cdot b_w \cdot f_{c,NSC})$ $m_{R1} = 0.5 \cdot x \cdot b_w \cdot f_{c,NC} \cdot \left(d - \frac{x}{3}\right) - 0.81 \cdot h_{UHPFRC} \cdot b_w \cdot f_{Ftu} \cdot \left(\frac{h_{UHPFRC}}{2} - (h_{slab} - d)\right) \quad (25)$	
Compression side	
$x = (A_s \cdot f_y + 0.81 \cdot h_{UHPFRC} \cdot b_w \cdot f_{Ftu}) / (0.5 \cdot b_w \cdot f_{c,UHPFRC} + 0.81 \cdot b_w \cdot f_{Ftu})$ $m_{R1} = 0.5 \cdot x \cdot b_w \cdot f_{c,UHPFRC} \cdot \left(d - \frac{x}{3}\right) - 0.81 \cdot (h_{UHPFRC} - x) \cdot b_w \cdot f_{Ftu} \cdot (d - 0.55 \cdot h_{UHPFRC} - 0.45 \cdot x) \quad (26)$	

Figure 6a shows the assumed stress distribution and internal forces on the cross-sections with UHPFRC distributed over the entire thickness. Figure 6b shows the locations from the resulting tensile force carried by the fibers upon reaching the ultimate limit state ( $F_{fd}$ ) assuming a more realistic stress distribution on the cross-section [1]. Figure 6c shows the equivalent stress blocks for Figure 6b that make the calculations more straightforward and provide similar flexural capacity results [1]. Similar assumptions described in Figure 9 were considered in evaluating the flexural capacity for cross-sections NSC-UHPFRC accounting for the thickness of the UHPFRC layer.

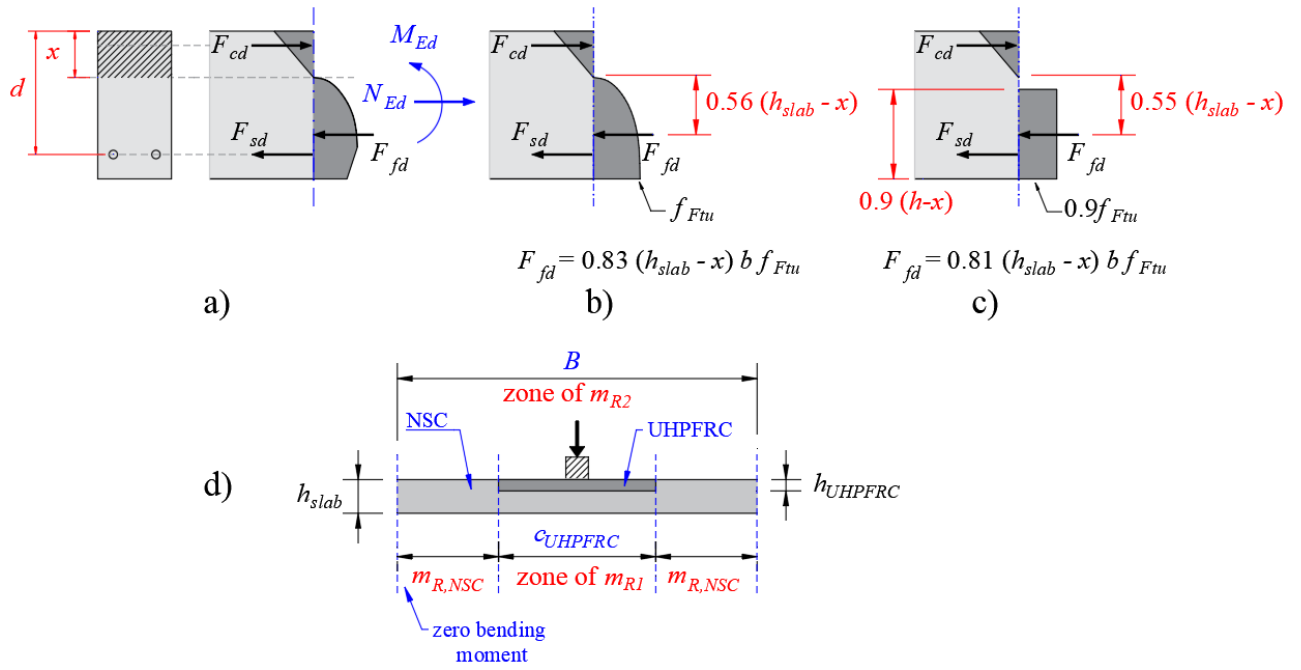


**Figure 6 - a) Stress distribution and resultant internal forces for the cracked cross-section; b) realistic stress distribution and resultant tensile force carried by the fibers upon reaching the ultimate limit state; c) stress blocks equivalent to b) (adapted from Fehling et al. [1]); and d) outlined regions with different flexural capacities and equivalent flexural capacities.**

The equations shown in Table 9 were used to predict the equivalent bending moment due to the different materials used over the slab thickness ( $m_{R1}$ ) in the region around the concentrated load (see Figure 6d). The unitary bending moment over the remaining region that contains only NSC ( $m_{R,NSC}$ ) was calculated according to Muttoni [41]:

$$m_{R,NSC} = \rho \cdot d^2 \cdot f_y \cdot \left( 1 - \frac{\rho \cdot f_y}{2 \cdot f_{c,NSC}} \right) \quad (27)$$

For slabs with the rational use of UHPFRC, the different distributions of UHPFRC over the slab plan were also accounted for (Figure 6d). The equivalent moment capacity per unit width  $m_{R2}$  at the support strip was calculated based on Gouveia et al. [36] by the following expression:

$$m_{R2} = \frac{m_{R1} \cdot c_{UHPFRC} + m_{R,NSC} \cdot (B - c_{UHPFRC})}{B} \quad (28)$$

where  $c_{UHPFRC}$  is the strip width of the UHPFRC region in the plan and  $B$  is the slab span length. In Table 9,  $f_{Ftu}$ , was calculated according to Hoang and Fehling [67]:

$$f_{Ftu} = 0.3 \cdot f_{c,UHPFRC}^{2/3} \quad (29)$$

The first investigated approach to predict the punching capacity of UHPFRC flat slabs, as well as NSC-UHPFRC flat slabs, was based on trying to adjust the failure criterion derived for SFRC from Maya et al. [68] using characteristics from the UHPFRC. The higher packing of UHPFRC compared to SFRC allows reaching enhanced bond factors  $k_b$  for straight steel fibers, such as used in the experiments by Zohrevand [14]. Supported by the experimental results from [74] and [75] with similar micro-coated steel fibers, the bond factor  $k_b$  was assumed equal to 1 in the calculations with the CSCT derived for SFRC [68]. In order to consider the thickness of the UHPFRC layer into the computed contribution from the fibers, the following expression was used:

$$P_{R,f,CSCT} = A_p \cdot \sigma_{tf} \cdot \left( \frac{h_{UHPFRC}}{h_{slab}} \right) \quad (30)$$

The term  $h_{UHPFRC}/h_{slab}$  was added to Eq. (30) to deal with the rational use of the UHPFRC over the slab thickness.  $h_{UHPFRC}$  and  $h_{slab}$  are the thickness of the UHPFRC layer and the slab thickness, respectively.

The second approach investigated was based on the modified failure criterion proposed by Moreillon [7], which suggests the following simplified failure criterion for UHPFRC flat slabs, also based on the CSCT:

$$P_{R,f,CSCT} = \frac{1}{K_{fo}} \cdot \frac{f_{Ftu} / \gamma_f}{1 + \frac{\psi_{CSCT} \cdot d}{w_u}} \cdot b_0 \cdot d \cdot \left( \frac{h_{UHPFRC}}{h_{slab}} \right) \quad (31)$$

where  $K_{fo}$  is the fiber orientation coefficient for general effects (taken equal to 1 for most applications [7]), and  $f_{Ftu}$  is the residual tensile strength at an ultimate crack opening  $w_u$ . For slabs that use only UHPFRC (for instance, U1.8 and U0.6),  $w_u$  assumed a value equals  $l_f/4$ , as suggested by Moreillon [7]. On the other hand, for specimens with the rational use of UHPFRC, the value of  $w_u = \psi_{CSCT} \cdot d/6$  suggested by Maya et al. [68] fitted better the experimental [14] and numerical results (Section 7). The different values of  $w_u$  were justified here because the deformation capacity of NSC-UHPFRC

flat slabs can be limited by the punching capacity from the outer region without UHPFRC, such as identified by Zohrevand et al. [14].

In order to account for the different contributions of the concrete ( $P_{R,c,C SCT}$ ) between the NSC and the UHPFRC, this parameter was weighted according to the thickness of the enhanced material in the slabs with the rational use of the UHPFRC:

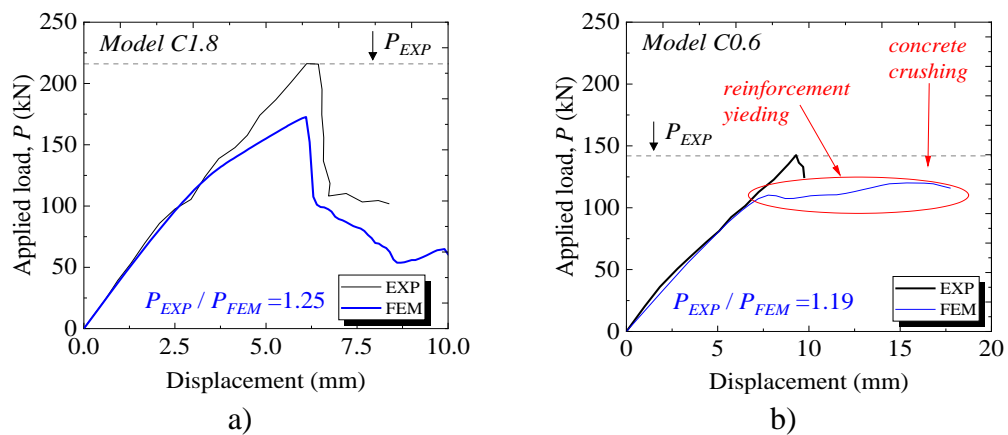
$$P_{R,c,C SCT} = \frac{3/4 \cdot \sqrt{f_{c,UHPFRC}}}{1 + 15 \cdot \frac{\psi_{C SCT} \cdot d}{d_{g0} + d_{ag}}} \cdot (b_0 \cdot d) \cdot \left( \frac{h_{UHPFRC}}{h_{slab}} \right) + \frac{3/4 \cdot \sqrt{f_{c,NSC}}}{1 + 15 \cdot \frac{\psi_{C SCT} \cdot d}{d_{g0} + d_{ag}}} \cdot (b_0 \cdot d) \cdot \left( 1 - \frac{h_{UHPFRC}}{h_{slab}} \right) \quad (32)$$

where  $f_{c,UHPFRC}$  and  $f_{c,NSC}$  are the compressive strengths of the UHPFRC and NSC, respectively.

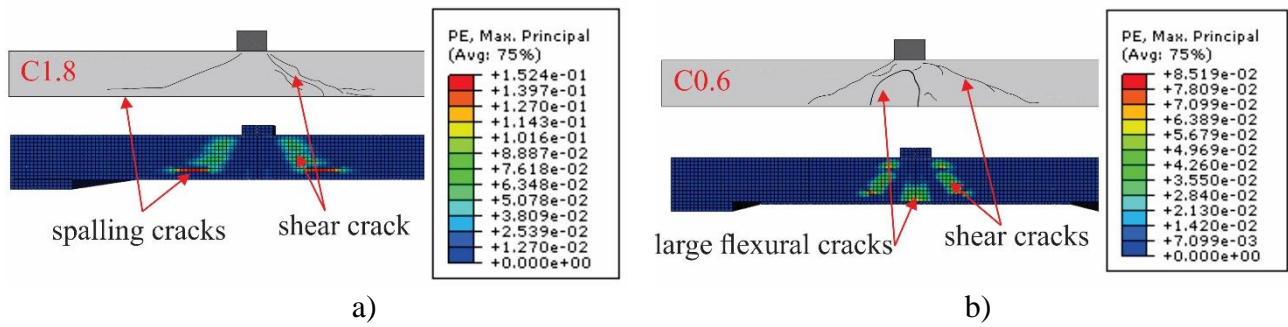
## 5 VALIDATION OF THE FEM AND MODELING CHOICES STUDY

### 5.1 Validation of the proposed FEM for NSC flat slabs

Figure 7 compares the FEM results with the experiments using NSC in terms of the punching capacity and failure mode. The proposed FEM reproduced reasonably well not only the punching capacity (Figure 7) but also the governing failure mode of the control slabs according to the cracking pattern (Figure 8). As described in reference [14], the slab C0.6 developed reinforcement yielding at failure (characteristic of flexure-induced punching) and C1.8 showed a brittle punching failure without yielding of the reinforcement at failure. Figure 8 confirms that the numerical models accurately predicted the cracking pattern and failure mechanisms of the specimens.



**Figure 7 - Comparison between load-displacement of experiment and NLFEM for a) C1.8 and b) C0.6.**



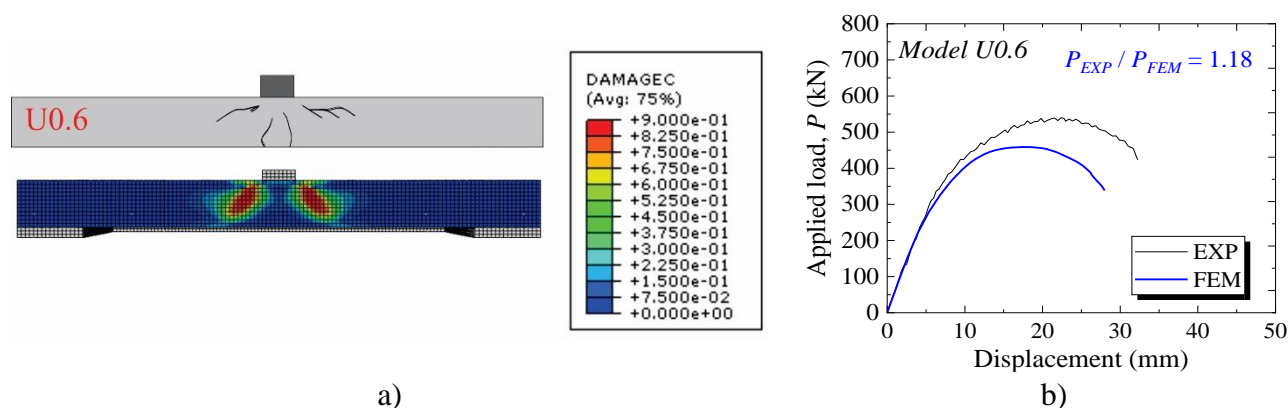
**Figure 8 - Comparison between crack patterns after the failure of experimental tests and NLFEA for a) C1.8 and b) C0.6. Note: PE is the tension plastic strain.**

Figure 7b shows that at failure, the FEM of the test C0.6 showed a slight drop in the measured punching force followed by an increase in capacity until a higher peak load. This behavior indicates that the FEM allowed load redistribution with the reinforcement yielding until reaching concrete crushing at the compression side of the slab. This behavior was not identified in the test because the test was potentially stopped when the first significant drop in the measured load occurred and major cracks had formed. Another explanation is that the tests may have been conducted by force control instead of displacement control. Therefore, some differences between the experimental and numerical graphs are reasonable for the post-peak load branch.

## 5.2 Validation of the proposed FEM for UHPFRC flat slabs

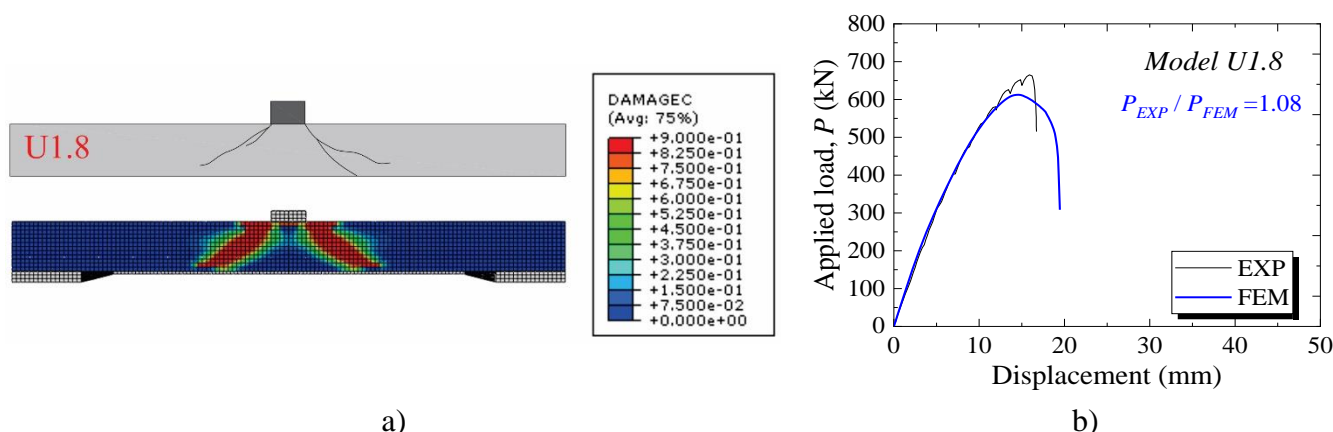
Figure 9 and Figure 10 compare test and numerical results in terms of crack pattern and predicted punching shear capacity for the flat slabs built with UHPFRC and different reinforcement ratios. The proposed NLFEA accurately predicted the crack pattern of U0.6 and U1.8 at the bottom side and in the cut views (Figure 9a and Figure 10a). The punching capacity predictions with the NLFEA differed from the experimental ones by less than 20%. The load-displacement graphs from the numerical models reproduced well the main characteristics observed at the tests: (i) punching capacity and (ii) yielding of the reinforcement prior to failure, (iii) the shape of the load-displacement graph in the non-linear branch for U0.6 (Figure 9b) and (iv) sharp decrease of the punching load after a certain degree of reinforcement yielding for U1.8 (Figure 10b). Since the cracking pattern based on the tensile damage (DAMAGET) of concrete for U0.6 and U1.8 was diffuse due to the higher post-peak tensile strength from the UHPFRC, the cracking pattern was evaluated at these FE models by

the compressive damage (DAMAGEC) in Figure 9a and Figure 10a. The results confirm that the failure mode of U1.8 was governed by reaching the full capacity of the compressive struts close to the loaded area.



**Figure 9 - Cracking pattern of slab U0.6 a) experimental test and numerical model; b) prediction of the punching capacity. Note: DAMAGEC is the damage variable in compression.**

The main differences between the experimental and numerical curves relate to the vertical displacements at failure. While the numerical model reached the maximum capacity at a displacement lower than the control experiment for U0.6 (Figure 9b), the numerical model of U1.8 failed at a higher vertical displacement than the experimental model (Figure 10c). Since the punching capacity and cracking pattern were well-represented by the numerical models, these differences in capturing the deflections at failure were considered acceptable. In this study, these differences can be related to the different stiffness of the support conditions used in the tests.



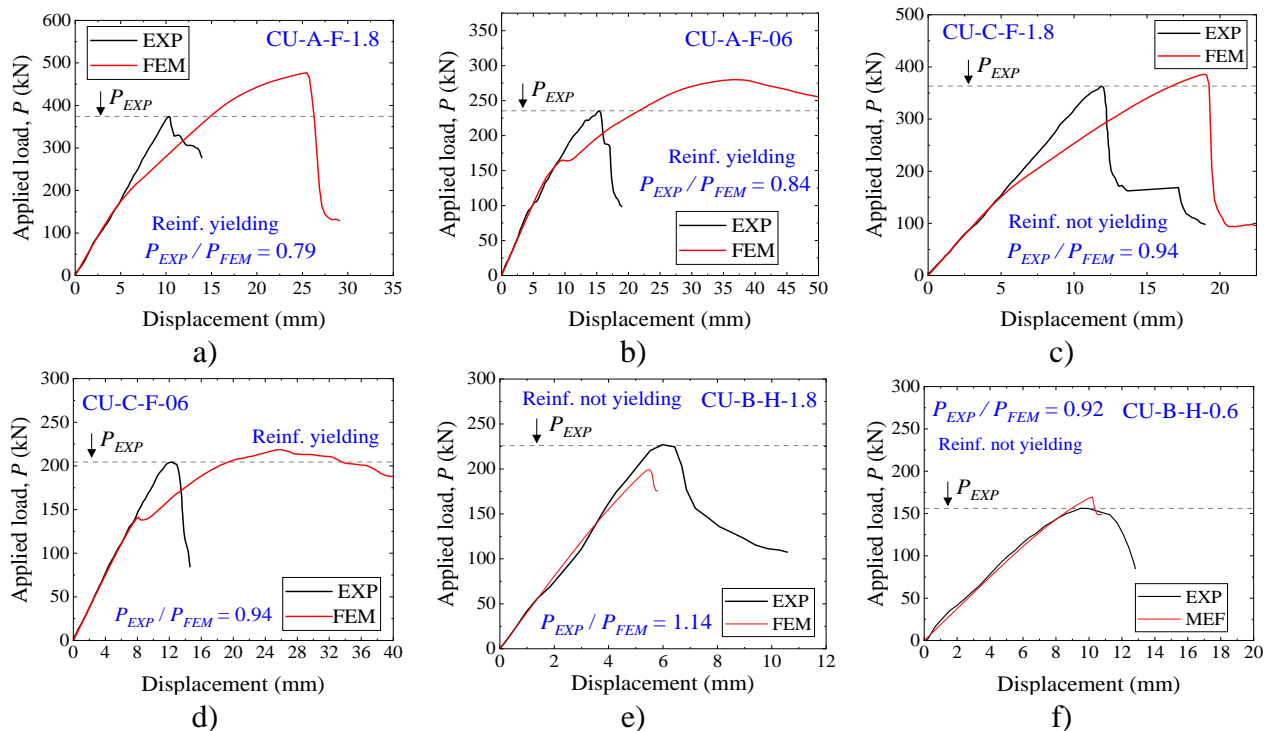
**Figure 10 – Cracking pattern and load-displacement graph of slab U1.8 a) experimental test and numerical model; b) prediction of the punching capacity. Note: DAMAGEC is the damage variable in compression.**

Figure 10 shows that the specimens with a higher amount of reinforcement (U1.8) failed at the struts that carry shear close to the loaded area, while the specimen with a lower reinforcement ratio (U0.6) failed by a combination of reinforcement yielding (softer decrease of the measured load) with the concrete crushing close to the loaded area. Proof that the UHPFRC material model was adequately represented in the FEM was that the governing failure mode of the tests was well-predicted despite the significant difference in the reinforcement ratios between slabs U1.8 and U0.6 and a relatively small difference in the punching capacities of these tests (22%).

## 6 PREDICTING THE PUNCHING CAPACITY OF NSC-UHPFRC FLAT SLABS

### 6.1 NLFEA results for NSC-UHPFRC-flat slabs

This section investigates the level of accuracy of the FEM proposed to describe the behavior of slabs with the rational use of UHPFRC at shear-critical regions (NSC-UHPFRC flat slabs). In this section, the material parameters described in Table 7 were used to model the non-linear behavior of NSC and UHPFRC, respectively.



**Figure 11 – Punching capacity predictions with the NLFEA for the members with the rational use of UHPFRC (NSC-UHPFRC flat slabs) tested by Zohrevand et al. [14].**

Figure 11 shows that the proposed material models for NSC and UHPFRC allowed predicting the punching capacity and the behavior of the hybrid flat slabs accurately. Since the tests from

Zohrevand et al. [14] may have been unloaded after reaching the maximum punching capacity, all reported force-displacement curves at failure could be misinterpreted as a brittle failure mode due to the sharp decrease of load at failure. Because of this, Figure 11 reports if reinforcement yielding was measured in the tests. Notably, when a brittle failure mode was observed in the control slabs, a sharp decrease of the load was also observed in the NLFE models at failure. Moreover, the finite element models captured reinforcement yielding of all control slabs that showed flexure-induced punching. The maximum error in the predicted punching capacities was 21%, which is within the mean error of material parameters such as the concrete tensile strength. Therefore, the level of accuracy reached was considered satisfactory.

Figure 12 shows that the FE models reproduced the cracking pattern in the control slabs at failure well. Minor differences were related to the development of the flexural crack at the interface between NSC and UHPFRC in some numerical models (Figure 12a), which were not identified for the control slabs.

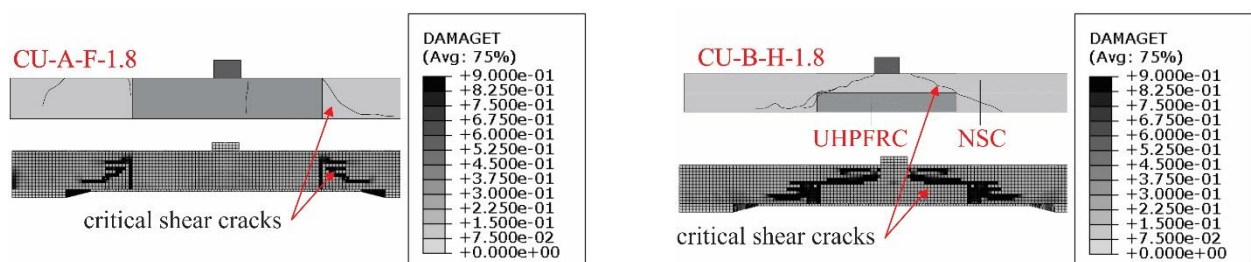


**Figure 12 - Comparison between crack patterns observed in the tests and in NLFE for CU-A-F-1.8 and CU-B-H-1.8. Note: DAMAGE is the damage variable in tension.**

The higher tensile damage at the shear crack in NSC indicates that the crack opening at the shear crack was higher than in the UHPFRC, despite the higher flexural action and shear concentration in the column vicinity. Consistently, no visible cracks were identified in the UHPFRC at failure [14]. This behavior may be related not only to the higher tensile and compressive strength of the UHPFRC compared to NSC but also to its capacity to redistribute inner forces due to its higher residual tensile strength after cracking.

## 6.2 Analytical results and comparison with NLFEA

Table 10 shows that the punching capacities predicted for NSC flat slabs (C1.8 and C0.6) with the CSCT [41] are similar to those predicted with NLFEA, such as shown by Millingan et al. [28] in similar analyses. However, limited information is available about the level of accuracy of the CSCT and NLFEA to predict the punching capacity of UHPFRC flat slabs [7]. Table 10 shows that the proposed NLFE models predicted well the punching capacity of the UHPFRC flat slabs. The values reached with the CSCT were more conservative using the failure criteria derived for SFRC [68], despite using some adjustments to account for the improved performance from the UHPFRC (Section 4.2) ( $P_{exp}/P_{calc}$  equal to 1.51 and 1.36, respectively for U1.8 and U0.6, see Table 10). However, improved predictions of the punching capacity were found using the simplified failure criteria proposed by Moreillon [7] ( $P_{exp}/P_{calc}$  equal to 1.25 and 1.26, respectively). Comparatively, the predictions with the semi-empirical model from Harris [11], whose results were reported in Zohrevand et al. [14] underestimated the punching capacities significantly for all tests. The model proposed by Harris [11] is inspired by ACI 318-11 [76] and was calibrated for experiments with unreinforced UHPFRC flat slabs. In this model, a shear cone starting from the column face and propagating at a  $34^\circ$  angle was assumed.

**Table 10 – Comparison between experimental and predicted punching capacities ( $P_{exp}/P_{calc}$ ) according to NLFEA, Harris [11], the CSCT models for SFRC [41,68], and modified for UHPFRC [7].**

Model	Grade	$P_{exp} / V_{FEM}$	$P_{exp} / V_{Harris}^a$	$P_{exp} / P_{CSCT}^b$	$P_{exp} / P_{CSCT}^c$
		NLFEA	Harris [11]	$P_{R,f,CSCT}$ by Maya [68]	$P_{R,f,CSCT}$ by Moreillon [7]
C1.8	Full depth	1.25	4.15	1.10	1.10
C0.6	Full depth	1.19	2.68	1.05	1.05
U1.8	Full depth	1.08	3.72	1.51	1.25
U0.6	Full depth	1.18	3.04	1.36	1.26
	AVG	1.17	3.40	1.25	1.16
	COV	6.1%	19.5%	17.1%	8.84%

<sup>a</sup>  $P_{Harris}$  values reported by Zohrevand et al. [14].

<sup>b</sup>  $P_{R,c,CSCT}$  given by eq. (16) and  $P_{R,f,CSCT}$  by eq. (20);

<sup>c</sup>  $P_{R,c,CSCT}$  given by eq. (16) and  $P_{R,f,CSCT}$  calculated by eq.(31);

Table 11 then shows a similar comparison for the control slabs with the rational use of UHPFRC in the region close to the loaded area. The contribution of  $P_{R,f,CSCT}$  was neglected for tests CU-B-H-1.8 and CU-B-H-0.6 since these did not develop a critical shear crack crossing the fibrous material [14]. This comparison shows that the proposed FE models accurately predicted the punching capacity. The mean ratio between experimental and predicted punching capacities was equal to 0.93 with a coefficient of variation (COV) of 13%, which is a reasonable value given the complexity of the problem and several parameters involved.

**Table 11 – Comparison between experimental and predicted punching capacities with the investigated approaches.**

Model	Grade	$P_{exp} / P_{FEM}$	$P_{exp} / P_{Harris}^a$	$P_{exp} / V_{CSCT}^b$	$P_{exp} / V_{CSCT}^c$
		NLFEA	Harris [11]	$P_{R,f,CSCT}$ by Maya [68]	$P_{R,f,CSCT}$ by Moreillon [7]
CU-A-F-1.8	Full depth	0.78	2.10	0.92	1.09
CU-A-F-0.6	Full depth	0.84	1.31	0.85	0.86
CU-C-F-1.8	Full depth	0.94	2.32	0.92	1.11
CU-C-F-0.6	Full depth	0.94	1.31	0.97	0.97
CU-B-H-1.8	Half depth	1.14	2.27	0.95	0.95
CU-B-H-0.6	Half depth	0.92	1.56	0.94	0.94
	AVG	0.93	1.81	0.93	0.99
	COV	13.0%	26.1%	4.44%	9.72%

<sup>a</sup>  $P_{Harris}$  reported by Zohrevand et al. [14].

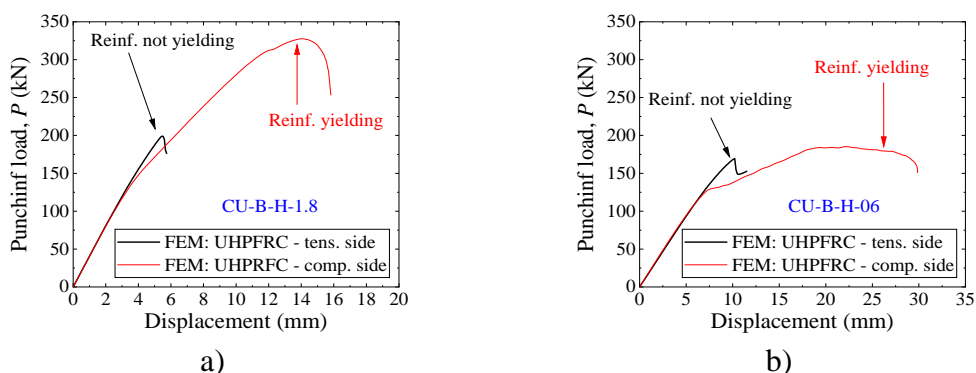
<sup>b</sup>  $P_{R,f,CSCT}$  calculated by eq. (20); <sup>c</sup>  $P_{R,f,CSCT}$  calculated by eq.(31);

Comparatively, this level of accuracy from the FEM was similar to that reported by Wu et al. [31] for a numerical study using the UHPFRC as an extra strengthening layer. Moreover, the predicted punching capacities with FEM were more accurate than semi-empirical approaches such as those proposed by Harris [11]. The predictions of the CSCT using the models from Maya [68] and Moreillon [7], adjusted for slabs with the rational use of UHPFRC, reached similar levels of accuracy to those provided by the NLFEA.

## 7 PARAMETRIC ANALYSES

### 7.1 Position of the UHPFRC on the slab depth

While some authors investigated the performance of hybrid slabs with the improved material at the tension side of the slab [14], others used it at the compression side [38]. Since the governing shear transfer action of mechanical punching shear models may vary between the aggregate interlock [41] and the compression chord capacity [77], the location of the enhanced material layer may influence the punching capacity differently accordingly for the reinforcement ratio of the slabs.



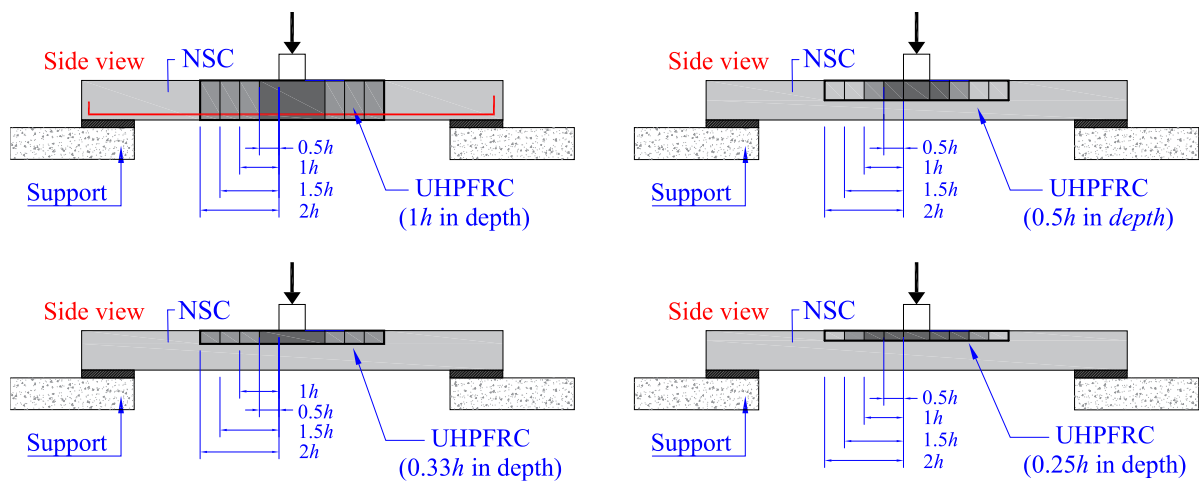
**Figure 13 – Effect of the location of the UHPFRC at the tension or compression side of the specimens a) CU-B-H-1.8 and b) CU-B-H-0.6. Note: Thickness of the enhanced material equal to  $0.5h$ .**

Figure 13a shows that placing the UHPFRC on the compression side for slabs with higher ratios of flexural reinforcement (CU-B-H-1.8) improves the punching capacity by around 64% compared to placing the UHPFRC at the tension side, and it increases the deformation capacity of the slab (ductility) markedly. For the slabs with a lower amount of flexural reinforcement (CU-B-H-0.6), the punching capacity did not change significantly comparing the two investigated options (Figure 13b). However, adding the UHPFRC on the compression side increased the deformation capacity of the slab-column connection. Since the flexure capacity is enhanced more efficiently with the UHPFRC placed at the tension side (see Table 9), this result was justified because placing the UHPFRC at the compression side hampers the development of the critical shear crack at failure more efficiently than placing the UHPFRC at the tension side of the slabs. Proof of this is that the critical

shear crack did not cross the UHPFRC in the tests CU-B-H-1.8 and CU-B-H0.6 from Zohrevand et al. [14].

## 7.2 Punching capacity enhancement with the rational use of UHPFRC

A parametric study was carried out to investigate the effect of different configurations of the UHPFRC layer placed in the shear-critical region for punching. In total, 48 numerical models were performed, varying the reinforcement ratio  $\rho$  (0.6%; 1.2% and 1.8%), the depth of the UHPFRC layer ( $0.25h$ ,  $0.33h$ ,  $0.50h$ ,  $1h$ ), and the size of the UHPFRC region in plan view (square areas with edges at a distance  $0.5h$  (configuration a),  $1h$  (configuration b),  $1.5h$  (configuration c) and  $2h$  (configuration d) from the column edges (Figure 14). The slabs had the geometry and support conditions of the hybrid slabs tested by Zohrevand et al. [14]. For these analyses, the material properties of the NSC were those of the slabs C1.8 and C0.6 tested by Zohrevand [14]:  $f_{cm} = 45$  MPa and  $d_{ag} = 9.5$  mm. The compressive strength and tensile strength of the UHPFRC were fixed as 140 MPa and 8 MPa, respectively, as previously studied. The material models used for both concretes are described in Table 7.



**Figure 14 – Configurations studied for the rational use of UHPFRC.**

Figure 15 shows that the use of enhanced material such as the UHPFRC increases the punching capacity regardless of the reinforcement ratios. The results of punching capacities enhancements herein reported are based on the comparison with the FEM predictions for specimens without UHPFRC (NSC flat slabs). The punching capacity enhancements varied between 26% and

156%, according to the reinforcement ratios and configurations of UHPFRC investigated. For the smaller thickness of the UHPFRC layer ( $0.25h$ ) and the minimum area covered around the column load ( $0.5h$  from the load edge), the punching capacity enhancements varied between 26% and 29% according to the reinforcement ratios. Using the UHPFRC layer over the entire slab thickness and in a square area of  $2h$  from the loading edges allowed reaching punching capacity enhancements of over 130% regardless of the reinforcement ratios.

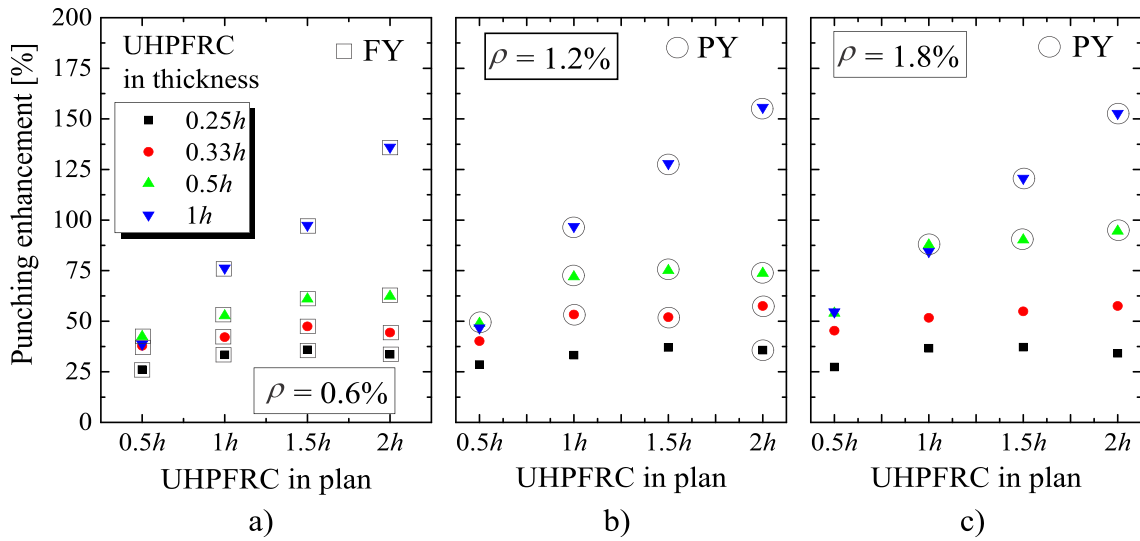


**Figure 15 - Punching capacity enhancements with the rational use of UHPFRC according to the UHPFRC layer thickness over the depth ( $0.25h$ ,  $0.33h$ ,  $0.50h$  and  $1h$ ), use of UHPFRC in plan (Figure 14) and for different values of the longitudinal reinforcement ratio: a)  $\rho = 0.6\%$ ; b)  $\rho = 1.2\%$ ; c)  $\rho = 1.8\%$ . Legend: FY and PY indicate punching failures with full (FY) and partial (PY) yielding of flexural reinforcement.**

However, different behaviors occurred according to the thickness of the UHPFRC layer. For the small thicknesses of the UHPFRC layer ( $0.25h$  and  $0.33h$ ), the increase of the UHPFRC layer in the horizontal plane did not significantly increase the punching capacity enhancements. On the other hand, when the UHPFRC layer was used over the entire slab thickness, the punching capacity enhancements increased almost linearly with the horizontal area of the UHPFRC layer, regardless of the reinforcement ratios. The increase of the punching capacity enhancements varied according to the reinforcement ratios for the slabs with the UHPFRC layer used at a half-thickness ( $0.5h$ ). For the

slabs with the smallest reinforcement ratio ( $\rho = 0.6\%$ ), the punching capacity enhancement increased from 42% to 62%, increasing the UHPFRC layer area from configuration  $0.5h$  to configuration  $2h$ . For the slabs with higher reinforcement ratios ( $\rho = 1.8\%$ ), the punching capacity enhancement varied between 54% and 94% according to the UHPFRC layer area.

As observed in the control tests from Zohrevand et al. [14], different punching failure mechanisms were identified in the parametric analyses according to the reinforcement ratios. All slabs with the smallest reinforcement ratio ( $\rho = 0.6\%$ ) developed flexure-induced punching failures with full yielding of flexural reinforcement (FY). The failure mode from slabs with  $\rho$  equal to 1.2% and 1.8% varied between brittle punching failures (without any reinforcement yielding) and punching failure with partial yielding of the flexural reinforcement (PY). Figure 15 indicates which tests developed reinforcement yielding at failure. Notably, most configurations studied developed partial or full yielding of the flexural reinforcement, which assures higher deformation capacity for such joints. Even though some specimens showed no signal of flexural yielding at failure, the deformation capacity increased compared to the control slabs. Therefore, the failure mode in the slab-column connections with the rational use of UHPFRC tends to be less brittle than in NSC slab-column connections.

### **7.3 Comparison between NLFEA and analytical predictions for NSC-UHPFRC slabs**

In daily engineering, analytical models are more practical for assessing problems such as the punching capacity in preliminary designs. In this section, the predicted punching capacities with the NLFEA in the parametric analyses (Section 7.2) were compared to those provided by the proposed analytical approach using the failure criteria from Moreillon [7] and the proposed adjustments for the rational use of UHPFRC (Section 4.2).

Figure 16 shows the comparison between numerical and analytical predictions of punching capacity according to the configuration of UHPFRC used in the slabs. The mean ratio between numerical and analytical punching capacities for the entire dataset, including 48 results, was 1.09 with a COV equal to 10.3%. These results indicate a close approximation between the NLFEA and

the mechanical punching shear model based on the CSCT. Therefore, the CSCT can be extended to the use of NSC-UHPFRC flat slabs in design practice.

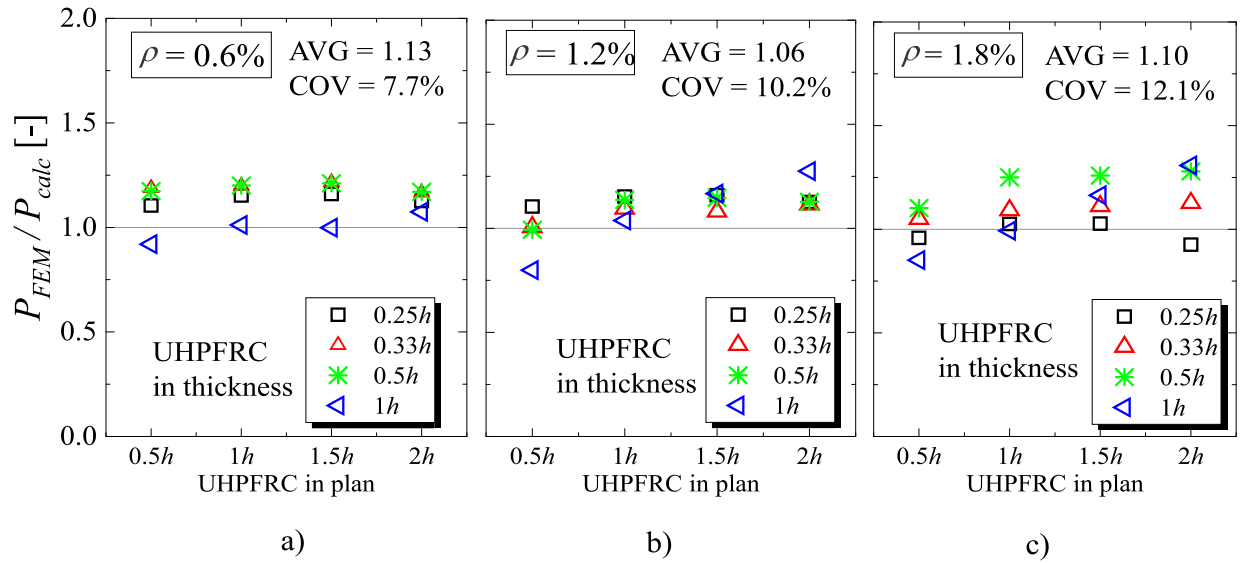


**Figure 16 - Comparison between numerical results and predicted punching shear capacities by the proposed approach for NSC-UHPFRC flat slabs: a)  $\rho = 0.6\%$ ; b)  $\rho = 1.2\%$  and c)  $\rho = 1.8\%$ .**

## 8 DISCUSSION

Only a limited number of studies have investigated the punching capacity of flat slabs with total depth [7,10] or the rational use of UHPFRC [14] at the shear-critical regions, which has hampered the spreading of this design practice. Notably, most studies make use of the UHPFRC only on the tension side of the slab [30,31,78–81]. At the same time, while modeling approaches are well established to investigate the behavior of flat slabs with NSC [20,21,24,25,28], similar guidelines for UHPFRC involving the CDP are scarce [30,31]. Furthermore, most of them were not validated to predict the behavior of UHPFRC-flat slabs since they used this material only as extra strengthening layer. Therefore, this paper provides a useful tool to suggest how the CDP model can be calibrated to model UHPFRC and then, after proper calibration, to extend the knowledge about the punching behavior of UHPFRC flat slabs and hybrid slabs (NSC-UHPFRC) through parametric studies.

The calibrated FEM predicted precisely the punching shear capacity and the governing failure mode of NSC, UHPFRC, and NSC-UHPFRC flat slabs. Compared to other studies that also modeled

UHPFRC with the CDP model [31,65,82–86], most of the input parameters used herein were derived from inverse analyses of experimental investigations [2,4], which increases the consistency of the selected parameters and the validity of the results. For instance, some authors proposed to use a dilation angle ranging from  $10^\circ$  to  $15^\circ$  due to the enhanced dense microstructure of the UHPFRC [85,87]. However, the inverse analyses of triaxial tests indicated that a value of  $54^\circ$  should be considered for modeling UHPFRC [2]. This occurs because the higher post-peak tensile strength from the UHPFRC increases the transversal deformation capacity of the material under high confining stresses.

Section 6 shows that the level of accuracy of the NLFEA proposed was similar to that provided with the CSCT for NSC flat slabs and UHPFRC flat slabs with the recommendations of Moreillon [7]. In contrast, the predictions with the modified CSCT [68] for SFRC provided more conservative predictions for UHPFRC flat slabs compared to the FEM results. This indicates that the behavior of UHPFRC flat slabs was not fully captured by the investigated approach, probably due to the higher toughness of UHPFRC compared to SFRC.

The parametric analyses (Section 7) indicate that placing the UHPFRC on the compression side of flat slabs is more efficient to improve the punching capacity of the slabs than placing the UHPFRC on the tension side of the slabs, mainly for those with higher reinforcement ratios (Figure 13a). Conversely, for slabs with lower reinforcement ratios (for instance,  $\rho = 0.6\%$ ), placing the UHPFRC on the tension or compression side did not enhance the punching capacity significantly (Figure 13b). However, the deformation capacity of the slabs with UHPFRC on the compression side for such cases was enhanced more efficiently. In summary, these results are in close agreement with those reported by Inácio et al. [38], which showed by analytical calculations with the CSCT that the beneficial effect provided by the enhanced material such as UHPC increases for higher reinforcement ratios. This behavior occurs because the punching strength is benefited in different ways increasing the reinforcement ratios: (i) the flexural stiffness of the slab increases, which decreases the slab rotations and corresponding crack openings; (ii) the interlocking strength is improved due to the lower

crack openings [38,41] and (iii) due to the enhanced fiber bridging stresses along the failure surface [7]. Consistently, the CSCT model allows considering all these effects.

The proposed approach to predict the punching capacity of NSC-UHPFRC slabs (Section 4.2), based on the works of Moreillon [7], Inácio et al. [38] and Gouveia et al. [36] using different types of materials, provided accurate predictions of punching strength for the slabs tested by Zohrevand et al. [14] (Section 6.2) and close predictions to advanced NLFEA developed in the parametric studies (Section 7.3). Therefore, the proposed approach may be used in the preliminary design for the punching capacity of flat slabs with the rational use of UHPFRC.

As suggestions for future works, the authors highlight that further experimental investigations should be performed to validate these results for other slab thicknesses and varying the material properties of NSC and UHPFRC.

## 9 CONCLUSIONS

This study investigated the level of accuracy of NLFEA performed with 3D continuum elements to predict the punching capacity and failure mode of three types of specimens: (i) flat slabs fully made of NSC, (ii) flat slabs fully made of UHPFRC and (iii) flat slabs with the use of UHPFRC only at a certain thickness of the slab and in the column vicinity. In the end, an analytical approach based on the CSCT was proposed to predict the punching capacity of hybrid slabs (NSC-UHPFRC slabs) with the rational use of UHPFRC, which was validated against experimental and numerical results.

### **From the parametric analyses, the following conclusions can be drawn:**

- Placing the UHPFRC at the compression side of slabs is more efficient to improve the punching capacity, mainly for slabs with higher reinforcement ratios. Furthermore, the slabs showed higher deformation capacity with the use of UHPFRC in the shear-critical regions, which is an additional benefit for the performance of flat slabs in seismic regions.
- The parametric analyses also indicated that the punching shear enhancement with the rational use of UHPFRC at the compression side of the slabs depends significantly on the geometry of the

UHPFRC layer. For slabs with reinforcement ratios of 1.8%, the punching capacity enhancement varied between 27% and 153%, changing the size of the UHPFRC layer (thickness and area around the loaded area). Although the higher punching capacity enhancements were reached using the UHPFRC over the entire thickness ( $> 100\%$  in some analyses), significant enhancements in the punching capacity were also reached with layers of small thickness ( $0.25h$  and  $0.33h$ ) placed at the compression side of the slabs.

**From the proposed analytical approach to predict the punching capacity, the following conclusions can be drawn:**

- The proposed approach based on the CSCT [41,68] and inspired by the works of Moreillon [7], Inácio et al. [38] and Gouveia et al. [36] leads to good predictions of the punching capacity of NSC-UHPFRC slabs with the rational use of UHPFRC around the loaded area and at the compression side. This statement is supported by comparisons between the analytical predictions and the experimental results of Zohrevand et al. [14], as well as by comparisons between the analytical calculations with advanced NLFEA developed in the parametric studies (Section 7.2 and Section 7.3).
- The bond factor  $k_b$  used to predict the punching capacity with the CSCT can be assumed equal to 1 due to the higher packing of the UHPFRC matrix, regardless of the fiber shape, when using the equations from Maya et al. [68] developed for SFRC. However, more accurate predictions were reached with the CSCT following the recommendations of Moreillon [7] to predict the punching strength of UHPFRC flat slabs with the CSCT: (i) estimating the ultimate crack opening  $w_u$  from a relation with the fiber length ( $w_u = l_f/4$ ); (ii) considering the higher post-cracking tensile strength in the punching capacity; and (iii) calculating the contribution of the fibers  $P_{Rf,CSCT}$  by Eq. (31).

In summary, the main significance of this research is that an economical and sustainable solution may be achieved by increasing the punching capacity of flat slabs without requiring stirrups with the rational use of UHPFRC. Since limited experiments are available about this kind of connection using this promising material [14], numerical studies may be a useful tool to extend the knowledge in this field. The importance of identifying analytical methods that are able to predict the

behavior of such joints is also highlighted, as such analytical methods are the main tools used in engineering practice. Therefore, the accurate predictions with the CSCT model with our proposed modifications should help to spread a design practice with the rational use of UHPFRC.

## ACKNOWLEDGMENTS

The authors acknowledge the financial support provided by the Brazilian National Council for Scientific and Technological Development (CNPq) and the São Paulo Research Foundation (FAPESP 2018/21573-2 and FAPESP 2019/20092-3).

## LIST OF NOTATIONS

Notation	Description
$A_p$	horizontally projected area of the punching shear failure surface
$B$	slab span length
$E_c$	modulus of elasticity of concrete
$E_s$	modulus of elasticity of the longitudinal reinforcement
$F$	load
$G_f$	Fracture energy
$G_c$	Crushing energy
$F_f$	Fiber factor
$K_c$	ratio of second stress invariants on tensile and compressive meridians (CDP)
$K_f$	global orientation factor for the Variable Engagement Model
$K_{f0}$	fiber orientation coefficient according to Model Code 2010 [55]
$P$	applied punching load
$P_{flex}$	shear force associated with flexural capacity of the slab
$P_{EXP}$	experimental punching capacity
$P_{calc}$	Predicted punching capacity by an analytical method
$P_{FEM}$	punching capacity predicted by the FE model
$P_{R,CSCT}$	punching capacity according with the CSCT [41,68]
$P_{R,c,CSCT}$	mean value of the concrete contribution to the punching capacity according to CSCT
$P_{R,f,CSCT}$	mean value of the fiber contribution to the punching capacity according to CSCT
$P_{Harris}$	punching capacity predicted by the expressions from Harris [11]
$V_f$	fiber volume content in percentage
$a_t ; b_t$	dimensionless coefficients from damage evolution models defined in [51]
$b_c$	dimensionless coefficients from damage evolution models defined in [52]
$b_0$	control perimeter of the critical section
$C_{load}$	size of square plate load
$C_{UHPFRC}$	strip width of the UHPFRC region in the plan
$c_1 ; c_2$	constants in the tension behavior model from Hordijk [50]
$d$	effective depth of the reinforcement considering both directions
$d_l$	effective depth of the reinforcement on the longitudinal direction
$d_t$	effective depth of the reinforcement on the transversal direction
$d_f$	fiber diameter
$d_{ag}$	maximum size of the aggregate
$d_{g0}$	reference aggregate size

$f_{cm}$	mean compressive strength of concrete (measured in cylinders)
$f_{c,UHPFRC}$	compressive strength of UHPFRC
$f_{c,NSC}$	compressive strength of NC
$f_{ct}$	concrete tensile strength
$f_{ct2,f}$	tensile stress in steel fiber-reinforced concrete for $w=3$ mm
$f_{Ftu}$	residual tensile strength at an ultimate crack opening $w_u$
$f_y$	average steel yield strength of the reinforcement
$h$	slab thickness
$h_{UHPFRC}$	thickness of the UHPFRC layer
$l_f$	Fiber length
$l_{eq}$	characteristics length related to the mesh size
$m, n, r$	dimensionless coefficients from damage evolution models in [4]
$m_R$	nominal moment capacity per unit width
$m_{R,NSC}$	nominal moment capacity per unit width of a RC strip using only NSC
$m_{R1}$	equivalent unitary moment capacity accounting for the distribution of UHPFRC in the slab thickness
$m_{R2}$	equivalent unitary moment capacity accounting for the distribution of UHPFRC in the slab plan
$m_s$	moment per unit width for calculation of the flexural reinforcement
$r_s$	distance from the column axis to the line of contra-flexure of the bending moments
$k_b$	bond factor
$k_1$ and $k_2$	experimental-based parameters related to the post-peak behavior of UHPFRC in compression [53]
$w$	crack opening
$w_c$	$w_c$ is the critical crack opening or fracture crack opening in [50]
$w_u$	ultimate crack opening, assumed equal to $l_f/4$ [7] for UHPFRC-flat slabs according to [7] and $\psi_{CSC} \cdot d/6$ for NSC-UHPFRC flat slabs
$x$	depth of the neutral axis
$\alpha_{cc}$	factor that accounts for long term effects on the compressive strength and unfavorable effects from the way load is applied
$\alpha_e$	fiber engagement parameter according Variable Engagement Model (VEM)
$\alpha_f$	fiber slenderness ( $l_f/d_f$ )
$\beta_{CC}$	factor that controls the post-peak branch of the compressive stress-strain model from Carreira and Chu [49]
$\beta_1$	factor relating depth of equivalent rectangular compressive stress block to neutral axis depth
$e$	flow potential eccentricity (CDP)
$\varepsilon_c$	total compressive strain
$\varepsilon_{cl}$	compressive strain corresponding to the peak compressive stress
$\varepsilon_t$	total tensile strength
$\varepsilon_{t,cr}$	tensile strain at peak tensile stress
$\varepsilon_c^{pl}$	plastic compressive strain
$\varepsilon_t^{pl}$	tensile plastic strain
$\varepsilon_{0c}^{el}$	elastic compressive strain
$\varepsilon_{0t}^{el}$	elastic tensile strain
$\varepsilon_c^{in}$	inelastic compressive strain
$\varepsilon_t^{in}$	inelastic tensile strain
$\rho$	average flexural reinforcement ratio
$\rho_l$ and $\rho_t$	flexural reinforcement ratios in longitudinal and transversal directions
$\rho_f$	fiber volume content

$\sigma_{b0}/\sigma_{c0}$	ratio of initial equibiaxial compressive yield stress to initial uniaxial compressive yield stress (CDP)
$\sigma_c$	compressive stress
$\sigma_{cf0}$	peak tensile strength of the UHPFRC
$\sigma_t$	tensile stress
$\sigma_{tf}$	fiber bridging stress
$\tau_f$	average fiber-matrix interfacial bond stress
$\psi_{CSCT}$	rotation of slab outside the column region in the CSCT
$\Psi$	Dilation angle for the concrete damaged plasticity model (CDP)
$\mu$	viscosity parameter (CDP)

## REFERENCES

- [1] Fehling E, Schmidt M, Walraven JC, Leutbecher T, Fröhlich S. Ultra-high performance concrete UHPC : fundamentals, design, examples. Ernst & Sohn; 2014.
- [2] Krah PA, Carrazedo R, El Debs MK. Mechanical damage evolution in UHPFRC: Experimental and numerical investigation. Eng Struct 2018;170:63–77. <https://doi.org/10.1016/j.engstruct.2018.05.064>.
- [3] Krah PA, de Miranda Saleme Gidrão G, Carrazedo R. Compressive behavior of UHPFRC under quasi-static and seismic strain rates considering the effect of fiber content. Constr Build Mater 2018;188:633–44. <https://doi.org/10.1016/J.CONBUILDMAT.2018.08.121>.
- [4] Krah PA, Gidrão G de MS, Carrazedo R. Cyclic behavior of UHPFRC under compression. Cem Concr Compos 2019;104:103363. <https://doi.org/10.1016/J.CEMCONCOMP.2019.103363>.
- [5] Graybeal BA. Compressive behavior of ultra-high-performance fiber-reinforced concrete. ACI Mater J 2007;104:146–52. <https://doi.org/10.14359/18577>.
- [6] Graybeal B, Brühwiler E, Kim B-S, Toutlemonde F, Voo YL, Zaghi A. International Perspective on UHPC in Bridge Engineering. J Bridge Eng 2020;25:04020094. [https://doi.org/10.1061/\(ASCE\)BE.1943-5592.0001630](https://doi.org/10.1061/(ASCE)BE.1943-5592.0001630).
- [7] Moreillon L. Shear strength of structural elements in high performance fibre reinforced concrete (HPFRC) 2013:480.
- [8] Al-Quraishi HAA. Punching Shear Behavior of UHPC Flat Slabs. Faculty of Civil and

- Environmental Engineering of the University of Kassel, PhD Thesis, 2014.
- [9] Nguyen TN, Nguyen TT, Pansuk W. Experimental study of the punching shear behavior of high performance steel fiber reinforced concrete slabs considering casting directions. *Eng Struct* 2017;131:564–73. <https://doi.org/10.1016/j.engstruct.2016.10.031>.
- [10] Shoukry ME, Tarabia AM, Yassin AM. Punching shear strength of ultra-high-performance fibre concrete slab–column connections. *Proc Inst Civ Eng - Struct Build* 2020;14:1–13. <https://doi.org/10.1680/jstbu.19.00201>.
- [11] Harris DK. Characterization of Punching Shear Capacity of Thin UhpC Plates. Virginia Tech, 2004.
- [12] Joh C, Hwang H, Kim B. Punching shear and flexural strengths of ultra high performance concrete slabs. *High Perform. Struct. Mater. IV*, vol. I, Southampton, UK: WIT Press; 2008, p. 97–106. <https://doi.org/10.2495/HPSM080111>.
- [13] Spasojevic A, Redaelli D, Muttoni A. Thin UHPFRC slabs without conventional reinforcement as light-weight structural elements. *fib Symp. London 2009*, London, UK: 2009, p. 8.
- [14] Zohrevand P, Yang X, Jiao X, Mirmiran A. Punching Shear Enhancement of Flat Slabs with Partial Use of Ultrahigh-Performance Concrete. *J Mater Civ Eng* 2014;27:04014255. [https://doi.org/10.1061/\(asce\)mt.1943-5533.0001219](https://doi.org/10.1061/(asce)mt.1943-5533.0001219).
- [15] Naaman AE, Likhitrungsilp V, Parra-Montesinos G. Punching shear response of high-performance fiber-reinforced cementitious composite slabs. *ACI Struct J* 2007;104:170–9. <https://doi.org/10.14359/18529>.
- [16] Pourbaba M, Joghataie A, Mirmiran A. Shear behavior of ultra-high performance concrete. *Constr Build Mater* 2018;183:554–64. <https://doi.org/10.1016/J.CONBUILDMAT.2018.06.117>.
- [17] Azmee NM, Shafiq N. Ultra-high performance concrete: From fundamental to applications. *Case Stud Constr Mater* 2018;9:e00197. <https://doi.org/10.1016/j.cscm.2018.e00197>.
- [18] Zhu Z, Yuan T, Xiang Z, Huang Y, Zhou YE, Shao X. Behavior and Fatigue Performance of

Details in an Orthotropic Steel Bridge with UHPC-Deck Plate Composite System under In-Service Traffic Flows. *J Bridg Eng* 2018;23:04017142. [https://doi.org/10.1061/\(asce\)be.1943-5592.0001167](https://doi.org/10.1061/(asce)be.1943-5592.0001167).

[19] R S, L. M. Punching shear strength of high performance fiber reinforced concrete slabs. 3rd FIB Int. Congr. Washingt., 2010.

[20] Genikomsou AS, Polak MA. Finite element analysis of punching shear of concrete slabs using damaged plasticity model in ABAQUS. *Eng Struct* 2015;98:38–48. <https://doi.org/10.1016/j.engstruct.2015.04.016>.

[21] Genikomsou AS, Polak MA. Finite-Element Analysis of Reinforced Concrete Slabs with Punching Shear Reinforcement. *J Struct Eng* 2016;142:1–15. [https://doi.org/10.1061/\(ASCE\)ST.1943-541X.0001603](https://doi.org/10.1061/(ASCE)ST.1943-541X.0001603).

[22] Genikomsou AS, Anna Polak M. Effect of openings on punching shear strength of reinforced concrete slabs-finite element investigation. *ACI Struct J* 2017;114:1249–62. <https://doi.org/10.14359/51689871>.

[23] Balomenos GP, Genikomsou AS, Polak MA. Investigation of the effect of openings of interior reinforced concrete flat slabs. *Struct Concr* 2018;1–10. <https://doi.org/10.1002/suco.201700201>.

[24] Genikomsou AS, Polak MA. 3D finite element investigation of the compressive membrane action effect in reinforced concrete flat slabs. *Eng Struct* 2017;136:233–44. <https://doi.org/10.1016/j.engstruct.2017.01.024>.

[25] Milligan GJ, Polak MA, Zurell C. Finite element analysis of punching shear behaviour of concrete slabs supported on rectangular columns. *Eng Struct* 2020;224:111189. <https://doi.org/10.1016/j.engstruct.2020.111189>.

[26] Navarro M, Ivorra S, Varona FB. Parametric finite element analysis of punching shear behaviour of RC slabs reinforced with bolts. *Comput Struct* 2020;228:106147. <https://doi.org/10.1016/j.compstruc.2019.106147>.

- [27] Navarro M, Ivorra S, Varona FB. Parametric computational analysis for punching shear in RC slabs. *Eng Struct* 2018;165:254–63. <https://doi.org/10.1016/J.ENGSTRUCT.2018.03.035>.
- [28] Milligan GJ, Polak MA, Zurell C. Impact of Column Rectangularity on Punching Shear Strength: Code Predictions versus Finite Element Analysis. *J Struct Eng* 2021;147:04020331. [https://doi.org/10.1061/\(ASCE\)ST.1943-541X.0002889](https://doi.org/10.1061/(ASCE)ST.1943-541X.0002889).
- [29] Marques MG, Liberati EAP, Pimentel MJ, de Souza RA, Trautwein LM. Nonlinear finite element analysis (NLFEA) of reinforced concrete flat slabs with holes. *Structures* 2020;27:1–11. <https://doi.org/10.1016/j.istruc.2020.05.004>.
- [30] Menna DW, Genikomsou AS. Punching Shear Response of Concrete Slabs Strengthened with Ultrahigh-Performance Fiber-Reinforced Concrete Using Finite-Element Methods. *Pract Period Struct Des Constr* 2021;26:04020057. [https://doi.org/10.1061/\(ASCE\)SC.1943-5576.0000546](https://doi.org/10.1061/(ASCE)SC.1943-5576.0000546).
- [31] Wu X, Yu S, Xue S, Kang TH-K, Hwang H-J. Punching shear strength of UHPFRC-RC composite flat plates. *Eng Struct* 2019;184:278–86. <https://doi.org/10.1016/J.ENGSTRUCT.2019.01.099>.
- [32] Kadhim MMA, Jawdhari A, Peiris A. Development of hybrid UHPC-NC beams: A numerical study. *Eng Struct* 2021;233:111893. <https://doi.org/10.1016/j.engstruct.2021.111893>.
- [33] Kadhim MMA, Saleh AR, Cunningham LS, Semendary AA. Numerical investigation of non-shear-reinforced UHPC hybrid flat slabs subject to punching shear. *Eng Struct* 2021;241:112444. <https://doi.org/10.1016/j.engstruct.2021.112444>.
- [34] Theodorakopoulos DD, Swamy N. Contribution of steel fibers to the strength characteristics of lightweight concrete slab-column connections failing in punching shear. *ACI Struct J* 1993;90:342–55. <https://doi.org/10.14359/3957>.
- [35] Cheng M-Y, Parra-Montesinos GJ. Evaluation of Steel Fiber Reinforcement for Punching Shear Resistance in Slab-Column Connections - Part I: Monotonically Increased Load. *ACI Struct J* 2010;107. <https://doi.org/10.14359/51663394>.

- 784 [36] Gouveia ND, Faria DM V., Ramos AP. Assessment of SFRC flat slab punching behaviour –  
 785 part I: monotonic vertical loading. *Mag Concr Res* 2019;71:587–98.  
 786 <https://doi.org/10.1680/jmacr.17.00343>.
- 787 [37] Gouveia ND, Faria DM V., Ramos AP. Assessment of SFRC flat slab punching behaviour –  
 788 part II: reversed horizontal cyclic loading. *Mag Concr Res* 2019;71:26–42.  
 789 <https://doi.org/10.1680/jmacr.17.00344>.
- 790 [38] Inácio MMG, Lapi M, Pinho Ramos A. Punching of reinforced concrete flat slabs – Rational  
 791 use of high strength concrete. *Eng Struct* 2020;206.  
 792 <https://doi.org/10.1016/j.engstruct.2020.110194>.
- 793 [39] Inácio M, Isufi B, Lapi M, Ramos AP. Rational Use of High-Strength Concrete in Flat Slab-  
 794 Column Connections under Seismic Loading. *ACI Struct J* 2020;117.  
 795 <https://doi.org/10.14359/51728080>.
- 796 [40] Qi J, Cheng Z, Zhou K, Zhu Y, Wang J, Bao Y. Experimental and theoretical investigations of  
 797 UHPC-NC composite slabs subjected to punching shear-flexural failure. *J Build Eng*  
 798 2021;102662. <https://doi.org/10.1016/j.jobe.2021.102662>.
- 799 [41] Muttoni A. Punching Shear Strength of Reinforced Concrete Slabs without Transverse  
 800 Reinforcement. *ACI Struct J* 2008;105:440–50. <https://doi.org/10.14359/19858>.
- 801 [42] Guandalini S, Burdet OL, Muttoni A. Punching tests of slabs with low reinforcement ratios.  
 802 *ACI Struct J* 2009;106:87–95.
- 803 [43] Abaqus 6.14. Abaqus Analysis User's Guide (6.14). Providence, Rhode Island: Dassault  
 804 Systems Simulia Corp.; 2014.
- 805 [44] Wei J, Wu C, Chen Y, Leung CKY. Shear strengthening of reinforced concrete beams with  
 806 high strength strain-hardening cementitious composites (HS-SHCC). *Mater Struct Constr*  
 807 2020;53:1–15. <https://doi.org/10.1617/s11527-020-01537-1>.
- 808 [45] Zhu H-G, Leung CKY, Cao Q. Preliminary Study on the Bond Properties of the PDCC  
 809 Concrete Repair System. *J Mater Civ Eng* 2011;23:1360–4.

810 [https://doi.org/10.1061/\(ASCE\)MT.1943-5533.0000296](https://doi.org/10.1061/(ASCE)MT.1943-5533.0000296).

811 [46] Sahmaran M, Yücel HE, Yildirim G, Al-Emam M, Lachemi M. Investigation of the Bond  
812 between Concrete Substrate and ECC Overlays. *J Mater Civ Eng* 2014;26:167–74.  
813 [https://doi.org/10.1061/\(ASCE\)MT.1943-5533.0000805](https://doi.org/10.1061/(ASCE)MT.1943-5533.0000805).

814 [47] Momayez A, Ehsani MR, Ramezani pour AA, Rajaie H. Comparison of methods for  
815 evaluating bond strength between concrete substrate and repair materials. *Cem Concr Res*  
816 2005;35:748–57. <https://doi.org/10.1016/j.cemconres.2004.05.027>.

817 [48] Nana WSA, Bui TT, Limam A, Abouri S. Experimental and Numerical Modelling of Shear  
818 Behaviour of Full-scale RC Slabs Under Concentrated Loads. *Structures* 2017;10:96–116.  
819 <https://doi.org/10.1016/j.istruc.2017.02.004>.

820 [49] Carreira DJ, Chu KH. Stress-strain relationship for plain concrete in compression. *ACI J*  
821 1985;82(6):797–804.

822 [50] Hordijk DA. Tensile and tensile fatigue behaviour of concrete — experiments, modelling and  
823 analyses. *Heron* 1992;37:3–79.

824 [51] Alfarah B, López-Almansa F, Oller S. New methodology for calculating damage variables  
825 evolution in Plastic Damage Model for RC structures. *Eng Struct* 2017;132:70–86.  
826 <https://doi.org/10.1016/j.engstruct.2016.11.022>.

827 [52] Birtel V, Mark P. Parameterised Finite Element Modelling of RC Beam Shear Failure.  
828 *Abaqus User's Conf.*, 2006, p. 95–108.

829 [53] Mansur MA, Chin MS, Wee TH. Stress-Strain Relationship of High-Strength Fiber Concrete  
830 in Compression. *J Mater Civ Eng* 1999;11:21–9. [https://doi.org/10.1061/\(ASCE\)0899-1561\(1999\)11:1\(21\)](https://doi.org/10.1061/(ASCE)0899-1561(1999)11:1(21)).

831

832 [54] Poliotti M, Bairán J-M. A new concrete plastic-damage model with an evolutive dilatancy  
833 parameter. *Eng Struct* 2019;189:541–9. <https://doi.org/10.1016/J.ENGSTRUCT.2019.03.086>.

834 [55] Fédération Internationale du Béton (fib). *fib Model Code for Concrete Structures* 2010. vol.  
835 1–2. Lausanne, Switzerland: Ernst & Sohn - fédération internationale du béton, Bulletin 65;

836 2012.

837 [56] CEB-Fip Model Code 1990. Design Code fib Fédération internationale du béton 1993.  
838 <https://doi.org/10.1680/ceb-fipmc1990.35430>.

839 [57] Kupfer H, Hilsdorf HK, Rusch H. Behavior of Concrete Under Biaxial Stresses. ACI J Proc  
840 1969;66:656–66. <https://doi.org/10.14359/7388>.

841 [58] Kupfer HB, Gerstle KH. Behavior of Concrete under Biaxial Stresses. J Eng Mech Div  
842 1973;99:853–66.

843 [59] Speck K. Beton unter mehraxialer Beanspruchung Concrete under multiaxial loading  
844 conditions. University of Dresden, 2008.

845 [60] Zohrevand P, Mirmiran A. Behavior of Ultrahigh-Performance Concrete Confined by Fiber-  
846 Reinforced Polymers. J Mater Civ Eng 2011;23:1727–34.  
847 [https://doi.org/10.1061/\(asce\)mt.1943-5533.0000324](https://doi.org/10.1061/(asce)mt.1943-5533.0000324).

848 [61] Babanajad SK, Farnam Y, Shekarchi M. Failure criteria and triaxial behaviour of HPFRC  
849 containing high reactivity metakaolin and silica fume. Constr Build Mater 2012;29:215–29.  
850 <https://doi.org/10.1016/j.conbuildmat.2011.08.094>.

851 [62] Öztekin E, Pul S, Hüsem M. Experimental determination of Drucker-Prager yield criterion  
852 parameters for normal and high strength concretes under triaxial compression. Constr Build  
853 Mater 2016;112:725–32. <https://doi.org/10.1016/j.conbuildmat.2016.02.127>.

854 [63] Lee JH, Hong SG, Joh C, Kwahk I, Lee JW. Biaxial tension–compression strength behaviour  
855 of UHPFRC in-plane elements. Mater Struct Constr 2017;50:1–17.  
856 <https://doi.org/10.1617/s11527-016-0918-1>.

857 [64] Zhu Y, Zhang Y, Hussein HH, Chen G. Numerical modeling for damaged reinforced concrete  
858 slab strengthened by ultra-high performance concrete (UHPC) layer. Eng Struct  
859 2020;209:110031. <https://doi.org/10.1016/j.engstruct.2019.110031>.

860 [65] Martín-Sanz H, Herraiz B, Brühwiler E, Chatzi E. Shear-bending failure modeling of concrete  
861 ribbed slabs strengthened with UHPFRC. Eng Struct 2020;222:110846.

- 862 <https://doi.org/10.1016/j.engstruct.2020.110846>.
- 863 [66] Felipe TRC, Leonel ED, Haach VG, Beck AT. A comprehensive ductile damage model for 3D  
864 truss structures. *Int J Non Linear Mech* 2019;112:13–24.  
865 <https://doi.org/10.1016/j.ijnonlinmec.2019.02.010>.
- 866 [67] Hoang A Le, Fehling E. Numerical analysis of circular steel tube confined UHPC stub  
867 columns. *Comput Concr* 2017;19:263–73. <https://doi.org/10.12989/cac.2017.19.3.263>.
- 868 [68] Maya LF, Fernández Ruiz M, Muttoni A, Foster SJ. Punching shear strength of steel fibre  
869 reinforced concrete slabs. *Eng Struct* 2012;40:83–94.  
870 <https://doi.org/10.1016/j.engstruct.2012.02.009>.
- 871 [69] Muttoni A, Ruiz MF, Bentz E, Foster S, Sigrist V. Background to *fib* Model Code 2010 shear  
872 provisions - part II: punching shear. *Struct Concr* 2013;14:204–14.  
873 <https://doi.org/10.1002/suco.201200064>.
- 874 [70] Muttoni A, Ruiz MF. The levels-of-approximation approach in MC 2010: Application to  
875 punching shear provisions. *Struct Concr* 2012;13:32–41.  
876 <https://doi.org/10.1002/suco.201100032>.
- 877 [71] Muttoni A, Fernandez Ruiz M. MC2010: the critical shear crack theory as a mechanical model  
878 for punching shear design and its application to code provisions. *FIB Bull. 57 Shear punching*  
879 *Shear RC FRC Elem., Lausanne (Switzerland): 2010*.
- 880 [72] Voo JYL, Foster SJSJ. Variable Engagement Model for the Fibre Reinforced Concrete in  
881 Tension. *Proc. Adv. Mater. Constr. Bridg. Build. Other Struct. III*, 2003, p. 86.
- 882 [73] Voo JYL, Foster S. Tensile-fracture of fibre-reinforced concrete: variable engagement mode.  
883 *6th Int RILEM Symp Fibre Reinf Concr* 2004:875–84.
- 884 [74] Lanwer J, Oettel V, Empelmann M, Höper S, Kowalsky U, Dinkler D. Bond behavior of micro  
885 steel fibers embedded in ultra-high performance concrete subjected to monotonic and cyclic  
886 loading. *Struct Concr* 2019;20:1243–53. <https://doi.org/10.1002/suco.201900030>.
- 887 [75] Denarié E, Habel K, Brühwiler E. Structural behavior of hybrid elements with Advanced

888 Cementitious Materials (HPFRCC). 4th Int Work High Perform Fiber Reinf Cem Compos  
889 2003:12.

890 [76] ACI Committee 318. Building code requirements for structural concrete (ACI 318-11) and  
891 commentary 2011.

892 [77] Marí A, Cladera A, Oller E, Bairán JM. A punching shear mechanical model for reinforced  
893 concrete flat slabs with and without shear reinforcement. *Eng Struct* 2018;166:413–26.  
894 <https://doi.org/10.1016/j.engstruct.2018.03.079>.

895 [78] Bastien-Masse M, Brühwiler E. Experimental investigation on punching resistance of R-  
896 UHPFRC–RC composite slabs. *Mater Struct Constr* 2016;49:1573–90.  
897 <https://doi.org/10.1617/s11527-015-0596-4>.

898 [79] Fiset M, Bastien J, Mitchell D. Methods for Shear Strengthening of Thick Concrete Slabs. *J*  
899 *Perform Constr Facil* 2016;31:04016103. [https://doi.org/10.1061/\(asce\)cf.1943-](https://doi.org/10.1061/(asce)cf.1943-)  
900 5509.0000960.

901 [80] Bastien-Masse M, Brühwiler E. Composite model for predicting the punching resistance of R-  
902 UHPFRC-RC composite slabs. *Eng Struct* 2016;117:603–16.  
903 <https://doi.org/10.1016/j.engstruct.2016.03.017>.

904 [81] Brühwiler E. UHPFRC technology to enhance the performance of existing concrete bridges.  
905 *Struct Infrastruct Eng* 2019;1–12. <https://doi.org/10.1080/15732479.2019.1605395>.

906 [82] Jang H-O, Lee H-S, Cho K, Kim J. Numerical and Experimental Analysis of the Shear  
907 Behavior of Ultrahigh-Performance Concrete Construction Joints. *Adv Mater Sci Eng*  
908 2018;2018:1–17. <https://doi.org/10.1155/2018/6429767>.

909 [83] Bahij S, Adekunle SK, Al-Osta M, Ahmad S, Al-Dulaijan SU, Rahman MK. Numerical  
910 investigation of the shear behavior of reinforced ultra-high-performance concrete beams.  
911 *Struct Concr* 2018;19:305–17. <https://doi.org/10.1002/suco.201700062>.

912 [84] Mahmud GH, Yang Z, Hassan AMT. Experimental and numerical studies of size effects of  
913 Ultra High Performance Steel Fibre Reinforced Concrete (UHPFRC) beams. *Constr Build*

- 914 Mater 2013;48:1027–34. <https://doi.org/10.1016/j.conbuildmat.2013.07.061>.
- 915 [85] Othman H, Marzouk H. Applicability of damage plasticity constitutive model for ultra-high  
916 performance fibre-reinforced concrete under impact loads. *Int J Impact Eng* 2018;114:20–31.  
917 <https://doi.org/10.1016/J.IJIMPENG.2017.12.013>.
- 918 [86] Fang C, Ali MSM, Sheikh AH, Singh M. Numerical and Finite-Element Analysis of Short  
919 Ultrahigh-Performance Fiber-Reinforced Concrete Columns. *J Struct Eng* 2019;145:1–17.  
920 [https://doi.org/10.1061/\(ASCE\)ST.1943-541X.0002389](https://doi.org/10.1061/(ASCE)ST.1943-541X.0002389).
- 921 [87] Chen L, Graybeal BA. Modeling Structural Performance of Ultrahigh Performance Concrete  
922 I-Girders. *J Bridg Eng* 2011;17:754–64. [https://doi.org/10.1061/\(asce\)be.1943-5592.0000305](https://doi.org/10.1061/(asce)be.1943-5592.0000305).
- 923